International Journal of Solids and Structures 80 (2016) 1–18

Contents lists available at ScienceDirect

International Journal of Solids and Structures

journal homepage: www.elsevier.com/locate/ijsolstr

Dynamic analysis of nano-heterogeneities in a finite-sized solid by boundary and finite element methods

S.L. Parvanova [a], G.P. Vasilev [a], P.S. Dineva [b], G.D. Manolis [c,*]

[a] Department of Structural Engineering, University of Architecture, Civil Engineering and Geodesy (UACEG) 1046 Sofia, Bulgaria
[b] Institute of Mechanics, Bulgarian Academy of Sciences (BAS), 1113 Sofia, Bulgaria
[c] Department of Civil Engineering, Aristotle University (AUTH), 54124 Thessaloniki, Greece

ARTICLE INFO

Article history:
Received 28 May 2015
Revised 12 October 2015
Available online 26 October 2015

Keywords:
Elastodynamics
Frequency domain analysis
Elastic solid matrix
Nano-cavities
Nano-inclusions
Boundary elements
Finite elements
Wave diffraction
Dynamic stress concentration

ABSTRACT

This work addresses the elastodynamic problem for a finite-sized, elastic solid matrix containing multiple nano-heterogeneities of arbitrary shape, number and geometric configuration. The problem is formulated under plane strain conditions, and time-harmonic motions are assumed to hold. The aim is to evaluate the non-uniform stress and strain fields that develop in the solid matrix and to identify zones of dynamic stress concentration for the case of dynamic loads applied along the matrix boundary. The mechanical model used here is based on a combination of classical elastodynamic theory for the bulk solid under non-classical boundary conditions, supplemented with a localized constitutive equation for the solid-inclusion interface in the framework of the Gurtin–Murdoch theory of surface elasticity. As computational tools we use (a) the 2D boundary element method (BEM) with frequency-dependent fundamental solutions for the bulk solid and (b) the finite element method (FEM) software package ANSYS augmented by a macro-finite element for representing surface effects on the contour of the nano-inclusions. At first, accuracy of the numerical solutions obtained for the dynamic stress concentration factor (DSCF) and for the diffracted displacement wave field is satisfactorily established. Next, comparison studies are conducted to gauge the BEM and FEM separately. These are followed by extensive numerical simulations that show that both BEM and FEM are able to capture the dependence of the diffracted wave field and of the DSCF on the type of the inclusions, their overall configuration and the nature of applied dynamic loads. It is concluded that the interaction effect between the nano-heterogeneities and the external perimeter of the bounded solid matrix is of paramount importance.
© 2015 Elsevier Ltd. All rights reserved.

1. Introduction

Wave propagation in homogeneous elastic continua is a well-known phenomenon and the numerical modeling effort involves solution of hyperbolic partial differential equations. The situation becomes far more complicated if the medium is heterogeneous, see Berezovski (2010). Elastic wave propagation through naturally occurring or man-made heterogeneous materials has attracted the attention of researchers from branches of science as diverse as seismology, material science, fracture mechanics, computational mechanics, etc. Another difficulty is that discontinuities such as cracks, cavities and inclusions complicate the overall picture by acting as scatterers and stress concentrators, thus causing reflection, refraction, diffraction and scattering phenomena that are not easy to quantify. In elastodynamics, the motion of waves in bounded solids is governed by the conservation law for linear momentum, the constitutive and kinematic relations, all complemented by initial as well as boundary continuity conditions along the solid boundaries, see Achenbach (1973). Computational tools available for solution of these problems within the frame of classical elastodynamics are as follows: (a) analytical and semi-analytical techniques dealing with regular geometries and employing wave function expansion methods (Kratochvil and Becker (2012), Li (2004), Pao and Mow (1971)), ray techniques (Babich (1956), Pao and Gajewski (1977)), complex function methods (Liu et al. (1982), Yang et al. (2015)), integral equation methods (Bostrom (2003), Lu and Hanyga (2004), Ayatollahi et al. (2009)), matrix methods including reflectivity methods and generalized coefficient techniques (Kennett (1983)), and finally mode matching techniques (Fah (1992), Panza et al. (2009)); (b) numerical techniques based on direct time and space discretization of the elastodynamic equations which lead to finite difference methods (Boore (1972), Kristek and Moczo (2003)) and finite element methods (Komatitsch et al. (2010), Nakasone et al. (2000), Santare et al. (2003), Wolf and Song (1996), Wolf (2003), Zhang and Katsube (1995)). The alternative use of integral representations based on reciprocity

* Corresponding author: Tel.: +30 2310995663; fax: +30 2310995769.
E-mail addresses: slp_fce@uacg.bg (S.L. Parvanova), gpekov@gmail.com (G.P. Vasilev), petia@imbm.bas.bg (P.S. Dineva), gdm@civil.auth.gr (G.D. Manolis).

http://dx.doi.org/10.1016/j.ijsolstr.2015.10.016
0020-7683/© 2015 Elsevier Ltd. All rights reserved.

theorems and the concurrent introduction of fundamental solutions of the governing differential equations leads to mesh reducing boundary element methods (Dominguez (1993), Dravinski and Yu (2011), Kausel (2006), Kobayashi (1983), Manolis and Beskos (1988), Manolis and Dineva (2015), Parvanova et al. (2013, 2014), Valeva and Ivanova (1998)); (c) hybrid techniques that combine the previously mentioned techniques in various ways (Dineva et al. (2012), Gatmiri and Arson (2008), Gatmiri et al. (2008), Manolis et al. (2015), Manolis and Dineva (2015), Mogilevskaya and Crouch (2001, 2002)).

During the last few years it has been recognized that the properties of a given material might not be primarily controlled by its chemical composition, but rather by its microstructure and more so by size ranging from nanometers to micrometers. The widely discussed in the literature size effect cannot be described by models in the framework of continuum mechanics and this demands the development of alternative models and of high-performance computational tools. When the characteristic cross-sectional dimension of a solid is in microns, the ratio of surface area to volume becomes an important parameter and the solid is strongly influenced by surface characteristics. These lead to distinct mechanical properties as compared with their bulk solid counterparts. With the rapid development of nanomechanical systems, size-dependent phenomena in the wave fields that develop in nanostructures with defects such as holes and inclusions are insufficiently understood and need further study. More specifically, variations in the surface energy in nanostructures are caused by relaxation of bonds between the surface atoms and this lead to formation of surface residual stress, which is something that does not happen inside the solid core. This behavior is a surface stress effect and is described in the surface elasticity model introduced by Gurtin and Murdoch (1975). It has been determined that surface stress is a summation of surface residual stress and surface elasticity. In Gurtin and Murdoch (1975), the interfaces between the nanoinhomogeneity and the matrix are regarded as 'thin' material surfaces that possess their own mechanical properties and surface tension. Furthermore, non-classical boundary conditions are derived for the tractions along an interface expressing a stress jump as we move from matrix to inclusion, due to the presence of surface stress related to the deformation-dependent surface energy. We note in passing that if the defects present in a material at the nanoscale are cracks, even more advanced mechanical theories must be used as surface effects will surely change the crack tip singularity values, see Sendova and Walton (2010).

A brief literature review for in-plane wave motion in heterogeneous nano-solids described by the Gurtin–Murdoch model points to the following: (a) most computational techniques used are actually analytical methods, and use of the boundary element method (BEM), which is most efficient for problems with low surface to volume ratios, is mostly absent (see Parvanova et al. 2015) for unbounded solids), except for static solutions. Also, the finite element method (FEM) is used to evaluate the contribution of surface stress to the total potential energy (see Wang et al. 2010) and the Gurtin–Murdoch surface stress model is implemented in commercial program ANSYS (2009) through its user programmable features. (b) There are no results for solution of in-plane wave diffraction problems in bounded heterogeneous solids at nanoscale; (c) in-plane diffraction of time-harmonic P- and SV- waves by nano-holes and nano-inclusions in unbounded solids were studied analytically in Ru et al. (2009), Wang et al. (2006), Wang (2009), and Zhang et al. (2011). More specifically, the wave function expansion method was used to derive analytical expressions for diffracted wave fields in the infinite elastic, isotropic plane with two circular holes in Wang (2009). Next, Wang et al. (2006) considered the diffraction of planar P- waves by a nano-sized circular hole using wave function expansion method. The same method was applied in Zhang and Katsube (1995) to study the diffraction of elastic waves by an array of cylindrical holes, including the effects of surface elasticity. The diffractions of planar P- and SV- waves by a cylindrical nano-cavity and nano-inclusion were investigated in Ru et al. (2009). Finally, Fang et al. (2010) analytically evaluated the presence of surfaces/interfaces on the dynamic stress around single circular hole, a single circular inclusion and two interacting circular nano-inclusions in an infinite matrix under P-waves.

A systematic study of the dynamic response of a finite elastic, isotropic solid with multiple heterogeneities at the nano-scale, which act both as wave scatterers and stress concentrators, seems necessary. To the authors' knowledge, the majority of current results in the field are for unbounded solids under static loads. In this respect, we believe that new results that take into account the interaction effect between the multiple inclusions and the external perimeter of the solid matrix at the nano-scale is both interesting and important. The present work is an effort in this direction and can be viewed as a continuation of our previous work (Parvanova et al. 2015) on the BEM modeling of wave scattering phenomena in an infinite elastic plane. Thus, we present new results for the interaction effect between the multiple nano-inclusions and the external perimeter of the elastic matrix.

More specifically, we focus on the 2D, time-harmonic elastodynamic problem for a finite, isotropic elastic solid at the nano-scale containing multiple heterogeneities of arbitrary configuration. To this purpose, we develop, verify and use for numerical simulations the following computational tools: (i) A BEM with 2D frequency-dependent fundamental solutions for the bulk solid; (ii) an FEM implementing of the surface effect on the contour of the nano-inclusion as one macro-finite element in the ANSYS (2009) software package. The paper is organized as follows: (a) we start with the formulation of the 2D elastodynamic problem for a finite, elastic and isotropic solid matrix with heterogeneous structure at the nano-scale solid under time-harmonic waves in Section 2; (b) we continue with a BEM reformulation at all interfaces to include surface effects in Section 3; (c) the FEM formulation and solution is developed in Section 4; (d) verification studies follow in Section 5 for the proposed numerical scheme; (e) comparison studies between the BEM and FEM follow in Section 6; (f) extensive parametric studies are conducted in Section 7 to investigate the effect of size-dependent effects in the solid matrix and finally (g) Section 8 lists the conclusions of the present study.

2. Problem statement

Consider wave motion in the plane $x_3 = 0$ for a Cartesian coordinate system $O\text{-}x_1x_2x_3$, where a finite-sized, elastic and isotropic solid with boundary Γ is subjected to time-harmonic loads with frequency ω, see Fig. 1. The solid matrix contains multiple nano-inclusions with boundaries Γ_I^n or nano-cavities Γ_H^n, where $n = 1, 2,\ldots, N$, of arbitrary shape, number, size and configuration. We assume that heterogeneities do not intersect and we denote their total surfaces as $\Gamma_I = \bigcup_{n=1}^{N} \Gamma_I^n$ and $\Gamma_H = \bigcup_{n=1}^{N} \Gamma_H^n$. The total boundary is then $S = \Gamma \cup \Gamma_H$ in the case of cavities (or holes) and $S = \Gamma \cup \Gamma_I$ in the case of inclusions. The material properties (Lamè constants and density) are denoted as λ_M, μ_M, ρ_M for the solid matrix and $\lambda_{I,n}, \mu_{I,n}, \rho_{I,n}$ for the nth inclusion. Furthermore, the displacement vector $u_i(x_1, x_2, \omega)$, (where $i, j = 1, 2$), the stresses $\sigma_{ij}(x_1, x_2, \omega)$ and the corresponding traction vector $t_i(x_1, x_2, \omega) = \sigma_{ij}(x_1, x_2, \omega)n_j$, ($n_j$ is the outward pointing unit normal vector) all satisfy the equations of motion in the bulk solid. In the absence of body forces, these are:

$$\sigma_{ij,i} + \rho\omega^2 u_j = 0 \tag{1}$$

where

$$\sigma_{ij} = \begin{cases} C_{ijkl}^{M} u_{k,l}^{M}(matrix) \\ C_{ijkl}^{I,n} u_{k,l}^{I,n}(n-th\ inclusion) \end{cases},$$

$$C_{ijkl} = \lambda\delta_{ij}\delta_{kl} + \mu(\delta_{ik}\delta_{jl} + \delta_{il}\delta_{jk}),\ \rho = \begin{cases} \rho_M \\ \rho_{I,n} \end{cases} \tag{2}$$

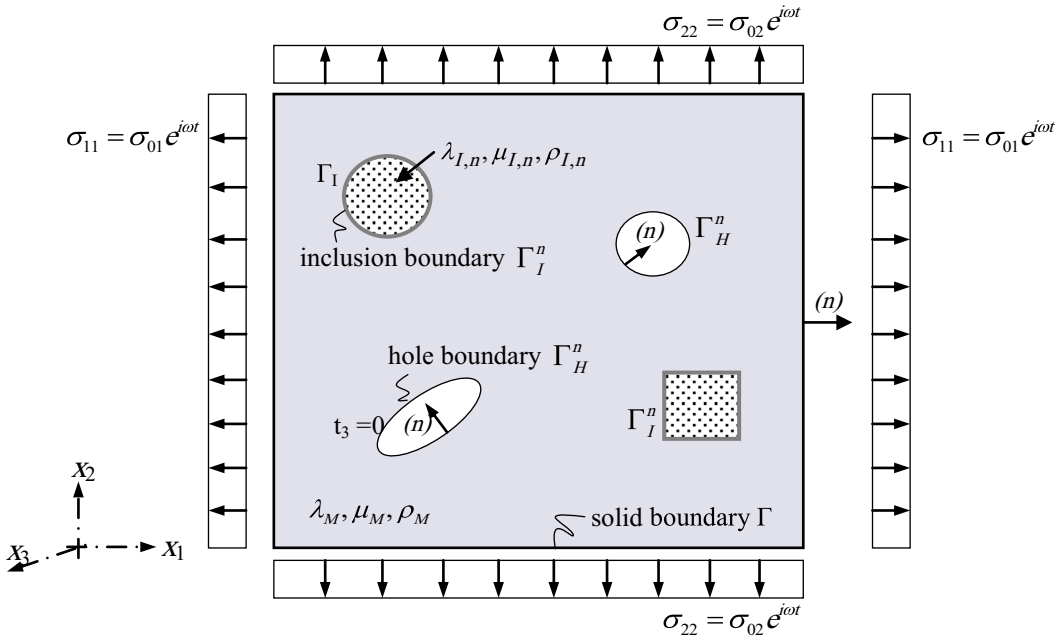


Fig. 1. Nano-cavities and nano-inclusions in a finite solid elastic matrix: problem layout.

In the above, comma subscripts denote partial differentiation with respect to the spatial coordinates and the summation convention over repeated indices is implied.

Following the surface elasticity theory of Gurtin and Murdoch (1975), the nth interface between a nano-inclusion and its surrounding elastic matrix is regarded as a thin material film with its own mechanical properties $\lambda^{S,n}, \mu^{S,n}$ and surface tension $\tau^{0,n}$. More specifically, $\tau^{0,n}$ is the residual surface tension under unstrained condition that will induce additional static deformation, which in dynamic analysis is usually ignored. We assume that all inclusion surfaces have the same material properties, denoted by λ^S, μ^S, τ^0. The constitutive equation along any interface Γ_I^M between the solid matrix and the corresponding inclusion is

$$\sigma^{sur} = \tau^0 + (2\mu^s + \lambda^s)\varepsilon^{sur} \tag{3}$$

In the above, $\sigma^{sur}$and $\varepsilon^{sur}$are the stress and the corresponding strain along the interface Γ_I^M, respectively. Next, the boundary conditions along Γ_I^M are as follows, see Dong and Pan (2011):

(a) Continuity of the displacement vector along any interface as seen from the side of the inclusion u_i^I and from the side of the surrounding matrix u_i^M in the $Ox_1x_2x_3$ coordinate system:

$$u_i^I = u_i^M = u_i;\ i = 1, 2 \tag{4}$$

(b) Interface equilibrium conditions along the arc length s, i.e., on the undeformed interface $s \equiv \Gamma_I^M$ written in terms of the local normal and tangential $(n,\ t)$ coordinates defined along s. These lead to the following relation between tractions along any interface coming from the side of the heterogeneity t_i^I and from the side of the surrounding matrix t_i^M, see Parvanova et al. (2015):

$$\begin{Bmatrix} t_1^I + t_1^M \\ t_2^I + t_2^M \end{Bmatrix}_k = \mathbf{f}_k^{sur} + \mathbf{T}_k^{sur} \begin{Bmatrix} u_1 \\ u_2 \end{Bmatrix}_k \tag{5}$$

Matrix $\mathbf{T}_k^{sur}$ and vector $\mathbf{f}_k^{sur}$ related with the kth node of the interface under consideration are derived as follows:

$$\mathbf{f}_k^{sur} = \left\{ -\frac{\tau_0}{\rho_s} \begin{Bmatrix} n_1 \\ n_2 \end{Bmatrix} \right\}_k \tag{6}$$

$$\mathbf{T}_k^{sur} = \begin{bmatrix} n_1 & -n_2 \\ n_2 & n_1 \end{bmatrix}_k \times \begin{bmatrix} \left(-\frac{\alpha}{(\rho_s)^2} + \tau^0 \frac{\partial^2}{\partial s^2}\right) & \left(\frac{-\alpha}{\rho_s}\frac{\partial}{\partial s} - \left(\frac{\tau^0}{\rho_s}\frac{\partial}{\partial s} - \frac{\tau_0}{(\rho_s)^2}\frac{\partial \rho_s}{\partial s}\right)\right) \\ \left(\left(\frac{-\alpha}{\rho_s}\frac{\partial}{\partial s} - \frac{\alpha}{(\rho_s)^2}\frac{\partial \rho_s}{\partial s}\right) + \frac{\tau^0}{\rho_s}\frac{\partial}{\partial s}\right) & \left(\alpha \frac{\partial^2}{\partial s^2} - \frac{\tau^0}{(\rho_s)^2}\right) \end{bmatrix}_k \times \begin{bmatrix} n_1 & n_2 \\ -n_2 & n_1 \end{bmatrix}_k \tag{7}$$

In the above, $n_1 = n_1^I = -n_1^M$; $n_2 = n_2^I = -n_2^M$ are the components of the normal vector as viewed from either side of an interface and ρ_s is the curvature radius for the corresponding interface s. As far as assigning numerical values to the surface constants for single-crystalline materials is concerned, these have been determined by either atomic simulations (Miller and Shenoy 2000; Shenoy 2002) or elaborate experiments (Jing et al. 2006). These results indicated that these surface constants depend on the material type and on the surface crystal orientation. Thus, a surface modulus that best captures interface effects at the nanoscale has been defined as $\alpha = K_S = 2\mu^S + \lambda^S$ in the papers by Dong and Pan (2011), Tian (2006), Tian and Rajapakse (2007), Ru et al. (2009), Wang et al. (2006) and Wang (2009). In the last two papers, a dimensionless parameter denoted as $s = K_S/2\mu a$, where a is the radius of the nanoinclusion and μ is the shear modulus of the bulk solid, is further used in the numerical simulations. The presence of a macroscopic inclusion with a large value of a leads to $s < <1.0$, which implies that surface effects can be neglected. However, when the radius of the inclusion shrinks to the nanoscale, s becomes noticeable and surface effect should be considered in analysis. For real nano-materials, the value of K_S is in the neighborhood of $\pm$ 10N/m, and negative values are also possible based on atomistic calculations (see Tian and Rajapakse 2007; Miller and Shenoy 2000).

In sum, the boundary-value problem (BVP) formulated above must satisfy the governing equations, Eq. (1), plus the continuity (or essential) boundary conditions of Eq. (4) and the equilibrium (or natural) boundary conditions of Eq. (5) along each interface Γ_I^M between a particular inclusion and the surrounding matrix. Note that if the membrane interface parameters $\tau^0 = 0$, $\lambda^S = \mu^S = 0$, then the

boundary condition of Eq. (5) transforms into the classical equilibrium condition for the traction vector. The aim now is to determine the dynamic stress-strain field at any point of the finite solid and the dynamic stress concentration factor (DSCF) along the perimeter of a nano-inclusion and a nano-cavity.

3. BEM formulation and solution

The BVP defined above can be reformulated (see Manolis and Beskos 1988) using a set of integral equations along the boundary S based on the Betti's reciprocity theorem, plus a set of frequency-dependent fundamental solutions for in-plane wave motion as follows:

$$c_{ij}u_j(\mathbf{x},\omega) = \int_S U^*_{ij}(\mathbf{x},\mathbf{y},\omega)t_j(\mathbf{y},\omega)dS(\mathbf{y}) - \int_S P^*_{ij}(\mathbf{x},\mathbf{y},\omega)u_j(\mathbf{y},\omega)dS(\mathbf{y}),\ \mathbf{x}\in S \tag{8}$$

In the above, c_{ij} are jump terms dependent on the local surface geometry at collocation point $\mathbf{x}(x_1, x_2)$, while U^*_{ij} is the displacement fundamental solution of Eq. (1) and $P^*_{ij} = C_{ijql}U^*_{qk,l}n_k$ is the corresponding traction fundamental solution. These surface integrals are either regular or singular, depending on whether or not the radial distance r between the source $\mathbf{y}$ and the receiver $\mathbf{x}$ points is zero. In the latter case, the displacement-based kernels exhibit a weak singularity of $O(\ln r)$, while the traction-based kernels exhibit a strong singularity of $O(1/r)$. Both regular surface integrals and those with weak singularity are computed using appropriate quadrature rules, while the strongly singular ones are evaluated by the rigid body motion concept. Finally, the displacements and stresses at any point inside the solid can be obtained from the well-known integral representation formulas, after the solution to Eq. (8) has been obtained.

Numerical solution of the system of the boundary integral equations (BIE) generated for all inclusions plus their surrounding finite solid matrix follows standard procedure, in the sense that all boundaries of the problem in question (in our case all interfaces $\Gamma^M_{I,j}$, $j = 1, 2,\ldots,N$ and the finite-sized solid with boundary Γ) are discretized using quadratic boundary elements (BE). Following a standard nodal collocation procedure, we get a system of linear algebraic equations in the form $\mathbf{Gt} = \mathbf{Hu}$, where $\mathbf{G}$ and $\mathbf{H}$ are global influence matrices, $\mathbf{t}$ and $\mathbf{u}$ are traction and displacement vectors at the nodal points. To this end, our BIE formulation is enhanced by sub-structuring capabilities, whereby it is possible to model inclusions plus the surrounding elastic matrix separately as if they were independently-occurring structures. The solution of the complete BVP is accomplished by enforcing displacement compatibility and traction equilibrium across all common boundaries.

In order to establish the nontrivial boundary conditions at any interface when we move to the nanoscale, a global $\mathbf{T}^{sur}$ matrix for each particular inclusion-matrix interface is defined. This matrix is composed by the individual nodal $\mathbf{T}^{sur}_k$ matrices for the kth node of the model defined by Eq. (7). Numerical evaluation of the $\mathbf{T}^{sur}$ matrix requires a more accurate approximation of the geometry and field variables at the nodal points so as to establish the relation between nodal tractions $\mathbf{t}$ and nodal displacements $\mathbf{u}$ in accordance with the nontrivial boundary conditions. This approximation, however, is not dependent on the original contour discretization which produced the BIE system matrices. In other words, standard BEM implementation can be realized with constant, linear or quadratic BE, but for the $\mathbf{T}^{sur}$ matrix evaluation we need a higher approximation of the geometry at the interfaces in order to accommodate the order of spatial derivatives required in Eq. (7). For that purpose we introduce a quartic (i.e., five-node) BE for approximation of the geometry, the displacements and the tractions at the interfaces. It is now possible to keep the same number of nodal points when modeling a closed surface, but when the nodal collocation technique commences, each source (i.e., central) node interfaces with the two advancing as well as with the two receding nodes, yielding spatial derivatives continuous to the fourth degree. This process is repeated until all nodes have been covered. The polynomial shape functions used for the quartic interface BE, as well as more details, are given in Parvanova et al. (2015).

4. FEM formulation and solution

In here, we apply the FEM for solving the above problem that requires a precise rendering of the surface effects along the contour of the nano-inclusions or the nano-cavities. In this work, we use the commercial software ANSYS (2009). This FEM environment does not have special type of elements for dealing with the surface effect, but it has user-programmable features (UPF) capabilities, which allow for the incorporation of any finite element (FE) developed outside the program. Thus, we develop an efficient macro-FE which models the boundary conditions along the interface contours. In the sections which follow, and for the sake of simplicity, we consider an elastic solid matrix with a single nano-inclusion, although the strategy for more nano-inclusions is the same.

4.1. Incorporation of surface effects

In classical continuum mechanics, the inclusion-matrix interface traction equilibrium condition is $(t^I_i + t^M_i)_k = 0$, where t^I_i and t^M_i are the traction forces at kth node along this interface, as viewed from either side, i.e., inclusion and elastic matrix in the ith direction, $i = 1,2$, respectively. For a nano-inclusion, the interface equilibrium condition, given by Eq. (5), holds for the kth node: $(t^I_i + t^M_i)_k = (f^{sur}_i)_k + (t^{sur}_{ij}u_j)_k$. We have that the vector $\mathbf{f}^{sur}_k = \{f^{sur}_i\}_k$ and the matrix $\mathbf{T}^{sur}_k = [t^{sur}_{ij}]_k$ for the kth node of the model, i,j=1,2, are dependent on the residual surface stress, the curvature and the orientation of the interface boundary. Obviously, the difference between classical and nontrivial equilibrium boundary condition is on the right-hand-side of both equations, which could be considered as an additional traction vector $\mathbf{t}^{add}_k = \mathbf{f}^{sur}_k + \mathbf{T}^{sur}_k\mathbf{u}$ for the kth node. In the case of the macroscale, this non-classical boundary condition degenerates to classical one, i.e., $\mathbf{t}^{add}_k = 0$. Similarly with the BEM implementation, we now have to obtain a proper relation between traction and displacement vectors at the entire interface. The derivation of a global $\mathbf{T}^{sur}$ matrix and a global $\mathbf{f}^{sur}$ vector for the entire interface is achieved by assemblage of the nodal $\mathbf{T}^{sur}_k$ and $\mathbf{f}^{sur}_k$ sub-matrices for all nodes of the contact contour, obeying the nontrivial boundary conditions as

$$\mathbf{t}^I + \mathbf{t}^M = \mathbf{t}^{add},\quad \mathbf{t}^{add} = \mathbf{f}^{sur} + \mathbf{T}^{sur}\mathbf{u} \tag{9}$$

In here, $\mathbf{t}^I$ and $\mathbf{t}^M$ are traction vectors along the entire interface viewed from the side of the inclusion and from that of the elastic matrix, $\mathbf{u}$ is the common displacement vector for the entire inclusion-matrix interface, and finally $\mathbf{t}^{add}$ is an additional traction vector due to the nontrivial boundary conditions at the nanoscale. The idea is to implement these additional tractions in the FEM model as a macro-FE described by a stiffness matrix and a load vector for all nodes belonging to the contact interface. To that purpose, we must convert Eq. (9) into nodal force-displacements relation. This means replacement of the interface tractions $\mathbf{t}^{add}$ with equivalent nodal forces $\mathbf{F}$ as follows:

$$\mathbf{F} = \mathbf{Mt}^{add} \tag{10}$$

In the above, matrix $\mathbf{M}$ is defined as $\mathbf{M} = \bigcup_e \int_{-1}^{1} \mathbf{N}^T\mathbf{N}Jd\xi$, J is the Jacobian of the transformation from local to global coordinates and ξ is an intrinsic coordinate. The matrix $\mathbf{M}$ components are numerically derived as a product of the traction shape functions for the eth FE along the interface under consideration, see Vasilev et al. (2015). In our previous BEM implementation, and in order to attain sufficient accuracy for curved geometries of arbitrary shape, a quartic (i.e., five-node) approximation for the geometry and field variables was used

in conjunction with the generation of the $\mathbf{T}^{sur}$ matrix. This higher order of approximation is mandatory for the derivation of the present transformation matrix $\mathbf{M}$, the nodal forces $\mathbf{F}$, and for the proper generation of the macro-FE. After substitution of $\mathbf{t}^{add}$ from Eq. (9) in Eq. (10) we get:

$$\mathbf{F} = \mathbf{M}\mathbf{f}^{sur} + \mathbf{M}\mathbf{T}^{sur}\mathbf{u}. \tag{11}$$

Here, vector $\mathbf{F}$ represents the additional nodal forces which account for surface effects at the inclusion-matrix interface.

4.2. Macro finite element formulation

A general methodology is presented here for the implementation of the surface effect as one macro-FE in the ANSYS (2009) software. We start with Eq. (11) that is identical to the well-known FEM formulation, i.e.,$\bar{\mathbf{F}} = \mathbf{K}\mathbf{u}$, where $\mathbf{K}$ is the stiffness matrix, $\mathbf{u}$ are displacements and $\bar{\mathbf{F}}$ is the load vector. Based on this expression and on Eq. (11), the macro-FE is introduced in a straightforward manner by a new stiffness matrix $\mathbf{K}$ and load vector $\bar{\mathbf{F}}$, created as follows:

$$\mathbf{K} = \mathbf{M}\mathbf{T}^{sur};\ \bar{\mathbf{F}} = -\mathbf{M}\mathbf{f}^{sur}. \tag{12}$$

It is worth mentioning that both matrix $\mathbf{K}$ and the vector $\bar{\mathbf{F}}$ are real-valued, independently of the type of analysis used. We can embed this macro-FE in any commercial software that allows element generation directly through importation of a stiffness matrix and a load vector. To this purpose, we activate the UPF option that offers many features to the programmer, one of which is macro-FE generation based on the stiffness, damping and mass matrices and on the element load vectors. Details about macro-FE implementation in an ANSYS (2009) environment can be found in Vasilev et al. (2015). In what follows, we implement macro-FE modeling directly in ANSYS (2009) for the problem of a square plate containing inclusions, which is a rather simple exercise. Finally, the discretized FE model and the imported macro-FE are coupled so as to satisfy the nodal compatibility and equilibrium conditions required for all active degrees-of-freedom (DOF) along the inclusion-matrix contact surface.

5. Verification study for the BEM

For our purposes, the available analytical and the majority of numerical solutions up to now are for infinite domains. In order to verify the proposed BEM scheme developed for finite regions, the size of the finite domain under consideration must be artificially extended to infinity with respect to the heterogeneity size. In all test examples, either nano-cavities or a single nano-inclusion are embedded in a finite square matrix. In order to achieve the best possible accuracy with the infinite plate solution, the solid matrix size is augmented to about one-hundred times the heterogeneity reference size.

5.1. Nano-scale elliptic cavity and inclusion in a square matrix under a static load

Consider a square matrix of size $100d$ containing either an elliptic cavity or an inclusion with semi-axes a and b, with $d = a + b$ and $a/b = 1.5$. The actual heterogeneity size is $d = 6.10^{-9}m$ for the case of the cavity and $d = 5.10^{-9}m$ for the inclusion. The solid matrix is an aluminium plate for the cavity case, with bulk elastic constants of $\lambda = 58.17\,\text{GPa},\ \mu = 26.13\,\text{GPa}$. For the nano-inclusion case, we consider a *GaAs-InAs* composite material with bulk Lame constant values for the matrix (i.e., *GaAs*) of $\lambda_M = 64.43\,\text{GPa}$, $\mu_M = 32.9\,\text{GPa}$ and with $\lambda_I = 50.66\,\text{GPa}$, $\mu_I = 19.0\,\text{GPa}$ for the inclusion (i.e, *InAs*). The excitation frequency is low and equal to $\omega = 10^{-4}\,\text{rad/s}$ in order to simulate quasi-static conditions. The surface stresses acting at the interface boundary are modeled as a thin film with surface elastic properties λ^S and μ^S, while the relevant surface effects are quantified by use of the material parameter $K_S = 2\mu^S + \lambda^S - \tau^0$. The special case of $\tau^0 = 0$ and $K_S = \pm 10\,\text{N/m}$ are adopted in the present verification study. The test examples used for comparison purposes were solved analytically by Tian (2006), who obtained a closed form analytical solution for the elastic field around a nanoscale inhomogeneity in an infinite matrix under far-field loading by using the complex potential technique of Muskhelishvili. This benchmark solution is for an infinite elastic plane with either a single, nano-scale elliptical cavity or an inclusion, under both far-field uniaxial $\sigma_{22}^{\infty} = \sigma_0$ and biaxial $\sigma_{11}^{\infty} = \sigma_{22}^{\infty} = \sigma_0$ loadings.

Moving on to the numerical implementation, the BEM used here mesh comprised 32 quadratic BE for the cavity perimeter and similarly for the matrix-inclusion interface boundary, and 64 quadratic BE for the square matrix, with 16 BE per side. A comparison between analytical solution of Tian (2006) and current BEM results is shown in Fig. 2(a) and (b) for the elliptic cavity, where the hoop stresses along the cavity perimeter are depicted for both loading types. Next, Fig. 2(c) and (d) plot the hoop stresses at the elliptic inclusion interface, as viewed from both solid matrix and nano-inclusion sides. As the analytical and numerical results are plotted concurrently for both uniaxial and biaxial far-field stress loadings, it is possible to observe the excellent agreement between the present BEM results and the analytical solutions. It is clarified here that the analytical results of Tian (2006) were directly reproduced from his own figures digitally and were not recomputed by the present authors.

5.2. Nano scale circular cavity and inclusions in a finite domain under a static load

In order to present a more quantitative comparison of current results with analytical ones, we consider the same square matrix as before, but now containing a circular cavity. A closed form solution for an infinite, linear elastic plane with a single nanoscale cylindrical hole is available in Grekov and Morozov (2012). The plane is under a far-field biaxial static stress load and the cavity has a fixed radius of $a_0 = 1.10^{-9}\text{m}$. The surface stresses that develop around the cavity boundary are modeled as a thin film with different values for the surface elasticity parameter K_S (in N/m), keeping at the same time the elastic properties of the surrounding elastic matrix fixed, i.e., $\lambda_M = 58.17\,\text{GPa},\ \mu_M = 26.13\,\text{GPa}$. Furthermore, plane strain conditions are assumed to hold and the far-field load is $t_1 = \sigma_0;\ t_2 = \nu(1-\nu)\sigma_0$, where ν is the Poisson ratio of the matrix. Again the special case of $\tau^0 = 0$ is used for verification purposes. Fig. 3 shows a comparison between the present BEM results and the analytical solution derived in Grekov and Morozov (2012). More specifically, the plots present the variation of the normalized stress ratio $\sigma_{\varphi\varphi}/\sigma_0$ at a fixed point on the cavity perimeter with polar angle $\pi/2$, versus surface parameter K_S. Three different BEM meshes are considered: (a) 8 quadratic BE for the cavity perimeter and 8 more BE for the square matrix edges; (b) 16 BE for each of these contours and (c) 32 BE for each of these contours. Furthermore, for more detail Fig. 3(b) presents the logarithmic (base 10) relative error (*RE*) between the BEM results for the three meshes and the analytical result, again versus surface parameter K_S. The relative error is defined as $RE = 1 - \sigma_{\varphi\varphi}(BEM)/\sigma_{\varphi\varphi}(analytical)$. We note that the source of numerical error in this example is also due to the fact that by using the BEM, we are trying to recover the analytical solution of an infinite domain by modeling a finite-size region. Furthermore, we reproduce static conditions indirectly by fixing the elastodynamic fundamental solutions at an extremely low circular frequency value of $\omega = 10^{-4}\,\text{rad/s}$. Despite these problems, the difference (as a percentage) between the BEM and the analytical solution at the observer point with polar angle $\pi/2$ range from 0.65% for the coarse mesh to 0.08% for the finer mesh, which is an acceptable level of accuracy.

The second verification example in this sub-section involves a finite metallic composite plate made of *GaAs*, containing two circular inclusions made of *InAs* with equal radii *R*, as shown in Fig. 4.

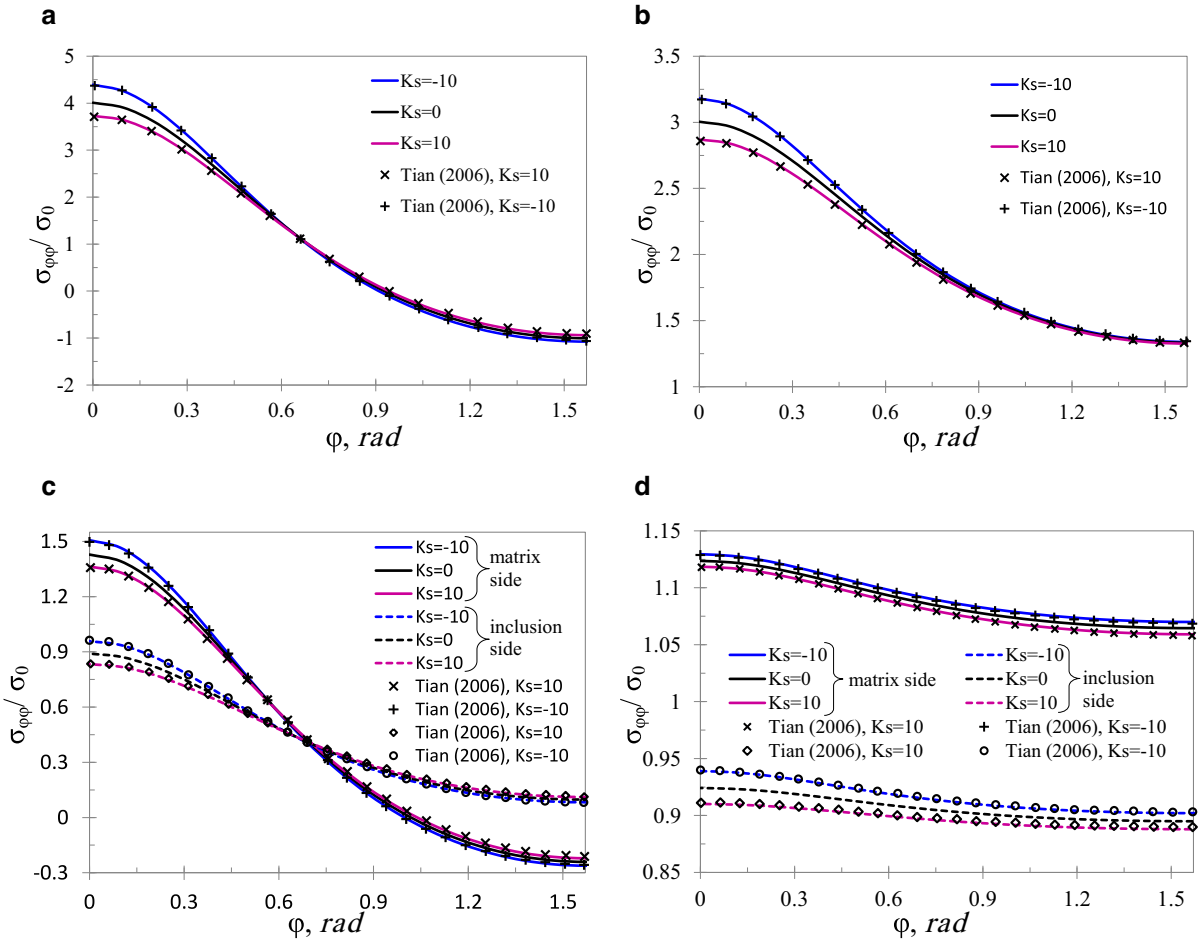


Fig. 2. Dimensionless hoop stress distribution around the (a) elliptic cavity perimeter under uniaxial loading $\sigma_{22}^{\infty} = \sigma_0$; (b) biaxial loading $\sigma_{11}^{\infty} = \sigma_{22}^{\infty} = \sigma_0$; (c) the elliptic inclusion-matrix interface under uniaxial loading $\sigma_{22}^{\infty} = \sigma_0$ and (d) biaxial loading $\sigma_{11}^{\infty} = \sigma_{22}^{\infty} = \sigma_0$.

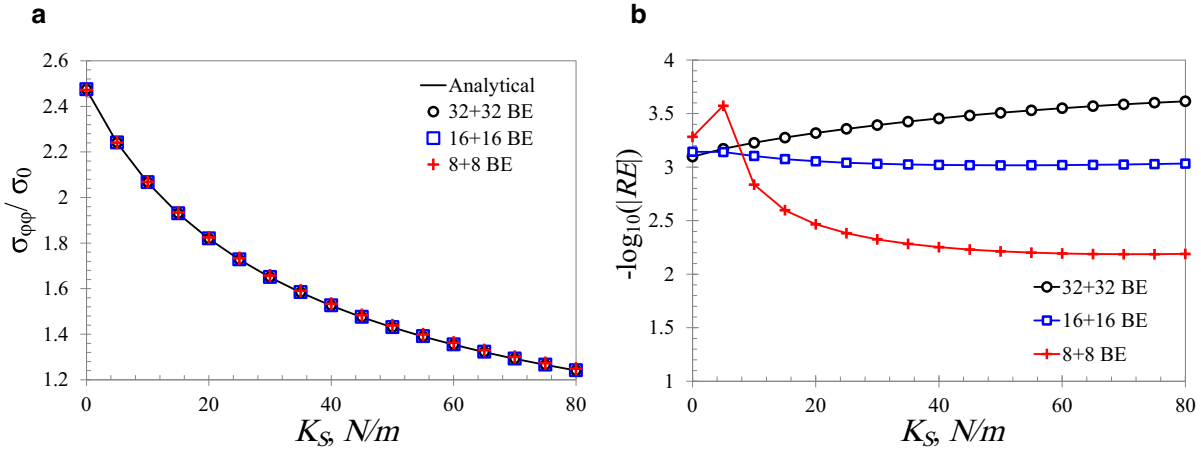


Fig. 3. (a) Dimensionless hoop stress at a fixed point on the circular cavity perimeter with polar angle $\pi/2$ versus surface parameter K_S and (b) logarithmic error estimate as a function of K_S.

The plate is subjected to uniform tension in the vertical direction. The layout of the inhomogeneities in the finite domain is depicted in Fig. 4(a), where we observe the inclusions located symmetrically in the plate at a centre-to-centre distance of 2*D*, where $D = 2R$, $L/R = 10$ and $H/R = 20$. This test example was solved numerically by Tian (2006), where the classical FEM was re-formulated so as to take into account the surface stress effect, while at the same time a FEM-based computer code was developed for numerical solution purposes. The variation of dimensionless hoop stresses along the inclusion-matrix interface at the right-side inclusion is now shown in Fig. 4(b) concurrently with the results of Tian (2006). These stresses are presented from both the matrix and the inclusion sides of the common interface, for two sub-cases: (i) an inclusion radius of $R = 5$ nm and a surface parameter value of $K_S = 10$ N/m and (ii) $R = 6$ nm with $K_S = -10$ N/m. Next, Fig. 4(c) and (d) depicts the variation of hoop stresses versus inhomogeneity radius in the matrix and right-side inclusion at

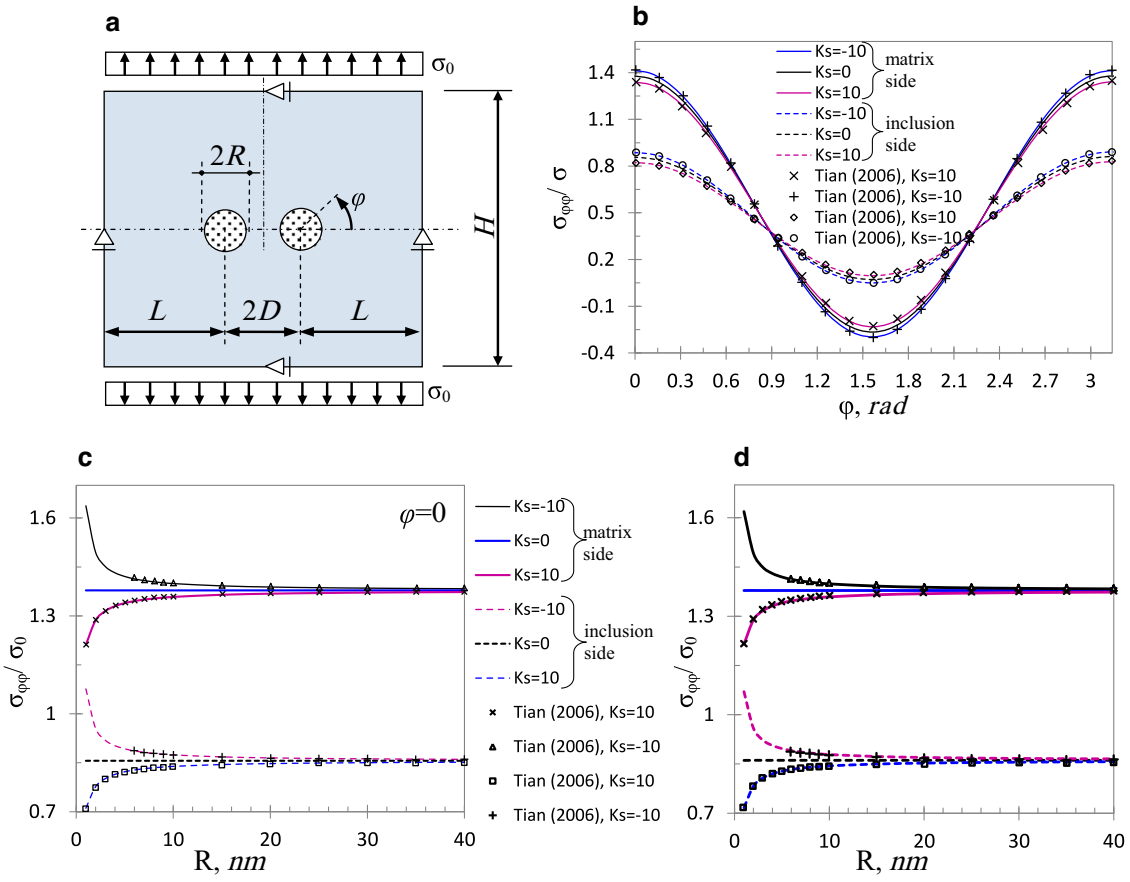


Fig. 4. Dimensionless hoop stress distribution at the nano-inclusion to matrix interface: (a) Problem layout; (b) stress versus polar angle; stress versus inclusion radius at fixed polar angles of (c) $\varphi = 0$ and (d) $\varphi = \pi$.

two polar locations corresponding to the equator ($\varphi = 0$, $\varphi = \pi$). In all cases, the results obtained by Tian (2006) are plotted concurrently with our BEM solutions. Again, we see good agreement in all cases. It is worth noting here that Tian (2006) observed that the stress distribution furnished by the FEM is unstable for negative values of K_S and for inclusion radii smaller than *7* nm. This, however, was not observed in our BEM solution, which is stable for the entire range of *1* nm–*40* nm for the inhomogeneity radius variation.

5.3. Nano-scale circular cavity in a square elastic matrix under a dynamic load

The final verification example is a comparison study between a finite square domain containing a circular nano- cavity of radius a_0, and the same nano-cavity in an infinite domain, both subjected to incident *P*-wave. This problem was originally solved analytically by Wang et al. (2006) using the displacement potential method and subsequently repeated for verification purposes by the present authors in Parvanova et al. (2015), where a BEM code was developed and used for modeling nano-heterogeneities in an infinite domain. The finite square domain considered here is of size $100a_0$. The numerical solution is in terms of the scattered displacement field, while the total displacement and stress fields are obtained by superposition of their respective scattered and incident field quantities. In order to ensure that no scattered displacements develop along the finite boundaries of the solid matrix, a 5% material damping is introduced, as opposed to Wang et al. (2006) solution.

The following notations are now introduced: (a) A dimensionless frequency parameter $\Omega = \omega\, a_0/C_P$, where C_P is the phase velocity of the propagating P-wave; (b) a dimensionless parameter $s = K_s/(2a_0\mu)$, with K_s previously defined and the shear modulus of surrounding medium, which serves to characterize surface effects; (c) a dynamic stress concentration factor defined as $DSCF_P = |\sigma_{\varphi\varphi}/\sigma_0|$, where $\sigma_0 = -\mu\, u_0\, C_S^2$ with $C_S = \sqrt{\mu/\rho}$ the shear wave velocity and u_0 the unit amplitude of the incoming wave. The residual surface tension τ^0 induces an additional static deformation, which is neglected in the present dynamic analysis. Finally, Poisson's ratio for the elastic medium is $\nu = 0.26$. The BEM numerical results are plotted in Fig. 5(a) and (b), concurrently for both finite and infinite domains, along with those given in Parvanova et al. (2015). More specifically, the DSCF is plotted along the interface boundary at two different dimensionless frequency values of $\Omega = 0.2$ and $\Omega = \pi$, when the incident P-wave is propagating in the positive Ox_1 direction. The BEM mesh used now comprises 32 elements for the interface at the low frequency value $\Omega = 0.2$ and 64 elements at the higher value $\Omega = \pi$. The same size of mesh is also used for the finite domain model's outer perimeter, but in this case the square domain is discretized with 64 BE for both frequency values. In closing, we again observe the good quality of our BEM results, as they are in agreement with those of Wang et al. (2006). Thus, all verification examples establish the correct BEM implementation at the nano-scale, which indirectly points to a correct FEM formulation for the macro-FE construction.

6. Comparison studies between BEM and FEM

The aim of this section is to establish the accuracy characteristics of the two different numerical methods developed herein for heterogeneous solid domains of finite extent at the nano-scale, namely the BEM and the FEM. To that purpose, the surface effect is implemented in the FEM ANSYS (2009) software by conversion of the $\mathbf{T}^{sur}$ matrix

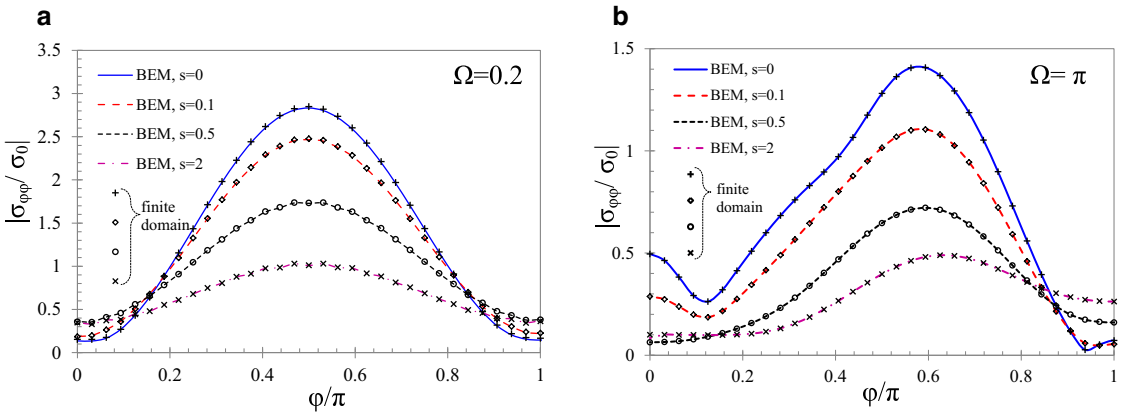


Fig. 5. DSCF for an incoming P-wave along the perimeter of a nano-cavity for both infinite and finite domains, for variable surface parameter s and at fixed non-dimensional frequencies of (a) $\Omega = 0.2$; (b) $\Omega = \pi$.

given in Section 4 into a single macro-FE, which is attached along the contact inclusion-matrix interface. The FEM results are compared with the ones obtained by already verified BEM software code in Section 5. The advantage of using an FEM commercial software packages, as compared to our in-house BEM code, is that they allow for solutions involving a solid finite matrix with anisotropic structure, or any other composition that is available in the ANSYS (2009) advanced element library.

6.1. Single nano-scale circular cavity in a square matrix under a dynamic load

As a first numerical example, we consider a square plate with a single circular cavity at its center under time harmonic tensile forces of magnitude σ_0 applied in horizontal direction, see Fig. 6(a). The diameter of the cavity is $d = 2a_0$ and the size of the square plate is $10d$. As before, a dimensionless parameter which captures interface effects at the nanoscale is defined as $s = K_S/(2\mu_M a_0)$, where μ_M is the shear modulus of the matrix material. In all simulations, the material damping is set to 5% and Poisson's ratio is 0.26. In order to avoid rigid body motion, four edge nodes belonging to the axes of symmetry are restrained. The difference in the results (as a percentage) that follow is calculated with respect to the average BEM/FEM values, since both are numerical methods and could be considered as having comparable accuracy.

In the ensuing numerical simulations, the BEM mesh employed comprises 64 BE, 32 for the cavity contour and 32 for the square matrix with 8 BE per side. The FEM mesh is structured so as to have 32 quadratic, planar FE along the cavity contour, which results in 64 boundary nodes so as to use an identical form of the $\mathbf{T}^{\mathbf{sur}}$ matrix in both methods. The plate edges are discretized into 40 FE and finally the entire mesh comprises 1876 quadratic, 8-noded plane FE (PLANE 82) augmented with the macro-FE. The results obtained by both numerical techniques are plotted in Fig. 6(b)–(d), where the dimensionless surface parameter value is fixed as $s = 0.5$, while the normalized frequency of vibration is $\Omega = \omega d/C_P = 0.24$. More specifically Fig. 6(b) depicts the normalized hoop stresses $|\sigma_{\varphi\varphi}/\sigma_0|$ versus polar angle φ, while Fig. 6(c) and (d) respectively plots the real and imaginary displacement components normalized as $u_i\mu_M/a_0\sigma_0, i = 1, 2$. The percentage difference in the normalized displacement components obtained by the BEM and FEM solutions ranges from 0.01 to 1.0% for most cases, but can reach up to *2%* for low values at the edges $\varphi = 0$ and $\varphi = \pi$. This percentage difference in the normalized stresses is in the range *0.005–4.4%*, and again the larger differences are observed when the stress values are low. In sum, the BEM and FEM convergence rates are different. If separate comparisons are made for two consecutive meshes as the discretization becomes finer, and at a fixed frequency value, then the differences observed in the displacements are less than 0.1% for both meshes.

Finally, a convergence study between the BEM and FEM results for the circular nano-cavity is presented in Fig. 7. More specifically, the Fig. 7 sub-plots (a)–(c) present the percentage difference in the results obtained by the BEM and FEM separately and both BEM/FEM numerical solutions. Five different BEM and FEM discretization schemes are used along the cavity perimeter employing 8, 16, 32, 64 and 128 quadratic-type boundary and finite elements. A parallel mesh refinement of the outer plate contour for each particular mesh has also been done, but for the purposes of the present comparison only the number of elements along the perimeter is important, as it directly influences the displacement and stress field recovery along the cavity contour. In more detail, Fig. 7(a) shows the fast rate of convergence between two successive meshes (e.g., 8 versus 16 BE, then, 16 versus 32, etc.) for the BEM solution, which is for the absolute values of the horizontal displacement component at polar angle φ=*0*, the amplitude of the vertical displacement component *at* $\varphi = \pi/2$ and the amplitudes of the hoop stresses at the same locations. A similar rate of convergence for the FEM solution is observed in Fig. 7(b). In quantitative terms, the differences in the BEM horizontal and vertical displacements between the two consecutive meshes of 32 and 64 quadratic BE are both 0.03% , while the same difference in the FEM displacements are 0.05% and 0.03%. Fig. 7(c) shows the percentage differences (calculated with respect to the averaged BEM/FEM numerical values) in the displacements and stresses from each pair of identical meshes. In all these sub-plots, the number of BE and FE used is plotted in logarithmic scale.

The last three plots in Fig. 7 quantify the logarithmic (base 10) relative difference (*RD*) (not the error as these are not analytical results) for the BEM and FEM separately and in combination. More specifically, the relative difference is defined as $RD = 1 - p(BE)/p(finest\ mesh)$, where $p(BE)$ is either $|u_1|$, $|u_2|$ or $|\sigma_{\varphi\varphi}/\sigma_0|$ for the particular BEM mesh identified by the number of BE along the cavity perimeter, while $p(finest\ mesh)$ is the analogous component under consideration recovered from the most detailed mesh available (here 128 elements per cavity) insofar as analytical results are not available for this example, see Fig. 7(d). The same comparison for the logarithmic (base 10) *RD* involving the FEM results is illustrated in Fig. 7(e). Finally, Fig. 7(f) plots the aforementioned *RD* between two identical (in terms of elements used) BEM and FEM meshes. Here the relative difference is defined as $RD = 1 - p(FEM)/p(BEM)$ where $p(FEM)$and $p(BEM)$ are the recovered $|u_1|$, $|u_2|$ and $|\sigma_{\varphi\varphi}/\sigma_0|$ values. In this last plot, the logarithmic (base 10) *RD* can be shown to be equivalent to the number of significant digits in either the BEM or FEM solutions.

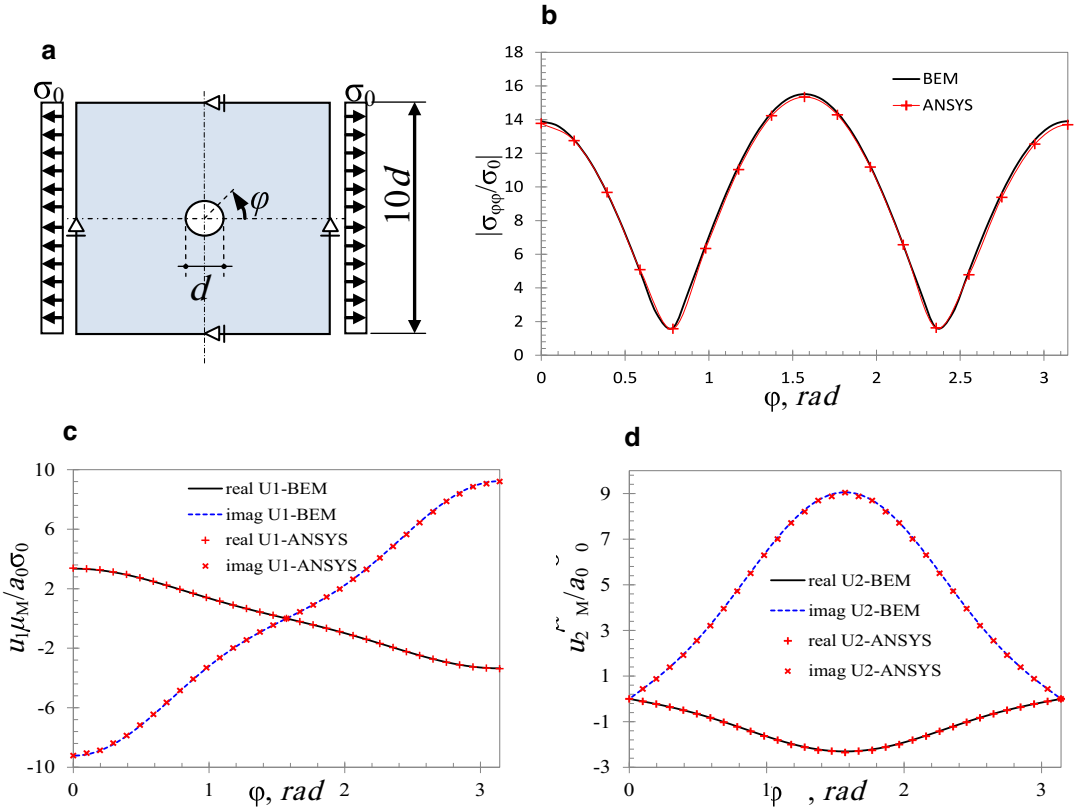


Fig. 6. Single circular cavity in a square matrix: (a) geometry and loading; (b) normalized hoop stresses; normalized (c) horizontal and (d) vertical displacement components versus polar angle, all along the cavity contour.

6.2. Single nano-scale circular inclusion in a square matrix under a dynamic load

The second numerical example is for a single circular inclusion in a square plate, see Fig. 8(a). The geometrical dimensions and loading are the same as in Example 6.1. The stiffness ratio of inclusion to matrix material is $\mu_I/\mu_M = 0.2$ and their respective densities yield a frequency ratio of$\Omega_I/\Omega_M = 3.0$, where $\Omega_I = \omega\, d/C_{P,I}$ and $\Omega_M = \omega\, d/C_{P,M}$, with $C_{P,I}$ and $C_{P,M}$ the phase velocities of the *P*-wave propagating in the inclusion and in the matrix medium. Poisson's ratio is the same for both inclusion and matrix, equal to $\nu = 0.26$.

The same discretization strategy as in Example 6.1 is used here, bringing the total to 2021 PLANE 82 FE in the model (plus the macro-FE and the inclusion domain). Note that the BEM mesh remains the same as in Example 6.1, as only surfaces are modeled. The results obtained by both BEM and FEM are now depicted in Fig. 8. More specifically, Fig. 8(b) plots the dimensionless hoop stresses at inclusion-matrix interface for a fixed surface parameter value of $s = 0.5$ and at a normalized frequency$\Omega_M = \omega\, d/C_{P,M} = 0.24$. Furthermore, Fig. 8(c) and (d) plots the horizontal and vertical displacement components along the inclusion-matrix interface, normalized by the matrix stiffness as $u_i\mu_M/a_0\sigma_0;\ i = 1, 2$. As before, excellent agreement between both solutions is observed, with the percentage error stemming from differences in the kinematic and in the stress field response being smaller than before for the cavity model.

6.3. Three nano-scale circular cavities or inclusions in a square matrix under a dynamic load

We now consider three circular cavities or inclusions embedded in a square solid matrix, as shown in Fig. 9(a). The aim here is to evaluate results obtained by both methods when multiple heterogeneities are embedded in the matrix, leading to interaction phenomena between them. The material properties, surface effect parameter and dimensionless frequency are the same as those used in Examples 6.1 and 6.2. In terms of discretization, the BEM mesh comprises 128 BE, 32 per each cavity contour and 32 for the plate perimeter. The corresponding FEM mesh comprises of 2100 quadratic FE when three circular cavities are present and 5479 quadratic FE when three circular inclusions are present. Next, in order to achieve plotting accuracy in the hoop stresses plotted in Fig. 10 when inclusions are present in the square matrix, the FEM mesh needs to be much finer than the corresponding BEM mesh. More specifically, the BEM model comprises 32 quadratic BE resulting in 64 nodal points at a single inclusion-matrix interface (as was the case for a cavity), while the FEM model for the same interface is modeled by 64 quadratic FE resulting in 128 nodes, which is double the refinement.

The normalized hoop stresses along the central and left cavity perimeters are presented in Fig. 9(b). Also, the normalized displacement amplitudes $|u_i|\mu_M/a_0\sigma_0$ in the case of cavities are depicted in Fig. 9(c) and (d). The normalized hoop stresses for the central and left inclusion-matrix interfaces, as viewed from the matrix and inclusion sides, are depicted in Fig. 10(a) and (b), respectively. Finally, Fig. 10(c) and (d) plots the normalized displacement amplitudes $|u_i|\mu_M/a_0\sigma_0$ for the central and left contact interfaces, respectively. We observe excellent agreement in the response furnished by both numerical methods for this complex problem. In sum, the percentage differences are of the same order as already reported in Example 6.1, reaching a maximum deviation of *1%* in the displacements and of *5%* in the stresses.

6.4. Single elliptic nano-scale cavity in a square matrix under a dynamic load

The last example in this section is for a nano-scale elliptic cavity in a square plate. We consider a relatively sharp ellipse with semi-axes

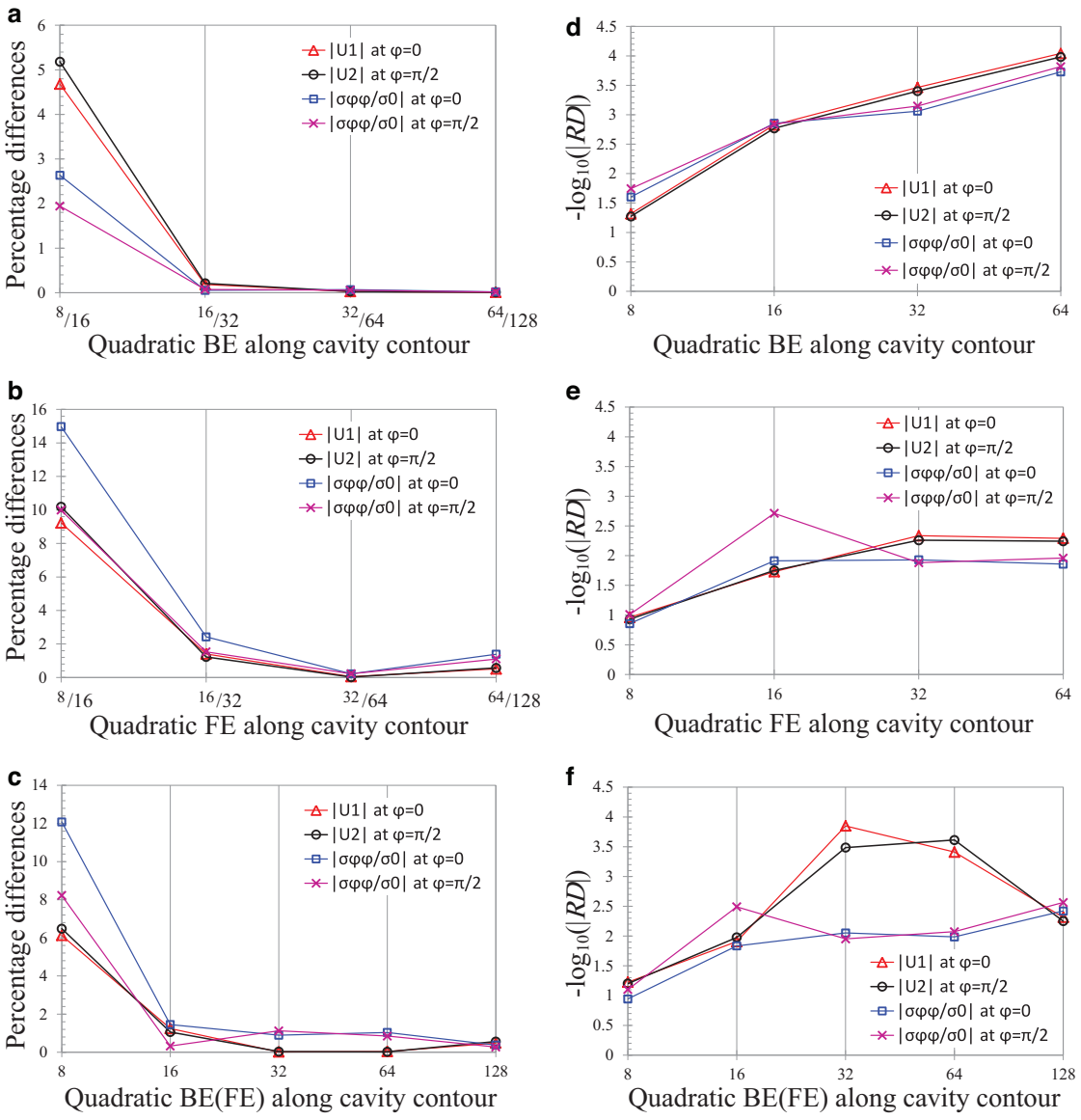


Fig. 7. Mesh convergence study between the BEM and FEM displacements and stresses for the case of a single circular nanocavity in a finite plate: (a)–(c) difference (as %) and (d)–(f) logarithmic difference, both versus cavity perimeter discretization.

dimensions a and b, with $d = a + b$ and a semi-axes ratio of $a/b = 3$. The size of the square plate is $20d$, see Fig. 11(a), while the dimensionless parameter which captures interface effects at the nanoscale now is defined as $s = K_S/(\mu_M d)$. In this example, the surface parameter value is relatively high, set to $s = 1$, and the normalized frequency is $\Omega = \omega\, d/C_P = 0.12$.

We note that the numerical accuracy level in the case of circular and elliptical nano-inhomogeneities, accounting for surface effects, is not the same and depends on the semi-axes ratio. The larger this ratio becomes, the more BE are needed in the model discretization. In order to verify the BEM accuracy and to find an optimal discretization scheme, several BEM solutions are tried involving 32, 64 and 128 BE for the elliptic cavity interface. Although the results obtained by numerical models with 64 and 128 BE along the cavity perimeter are practically identical, those obtained with 32 BE give different hoop stress distributions at the sharp edge of the ellipse. A similar picture is observed in the horizontal displacement components at the sharp edge, but there the discrepancies are minor, while for the stresses they are significant. As far as the FEM model is concerned, the cavity perimeter is discretized using 128 quadratic planar FE, which results in 256 nodal points and 5739 elements for the whole model.

In terms of results, the normalized hoop stresses along the cavity perimeter, as obtained by both BEM and FEM, are plotted in Fig. 11(b). Also, the normalized displacement amplitudes $|u_i|\mu_M/d\sigma_0$ at the cavity interface are depicted in Fig. 11(c). As with the previous examples, an excellent level of agreement is reached for the numerical results obtained by both methods.

7. Parametric studies

This final section collects numerical results from a series test examples involving multiple nano-cavities and nano-inclusions within a finite, elastic matrix in order to quantify DSCF dependence to the following key factors: (a) type, size and shape of the nano-heterogeneity; (b) ratio of the material bulk properties of the solid

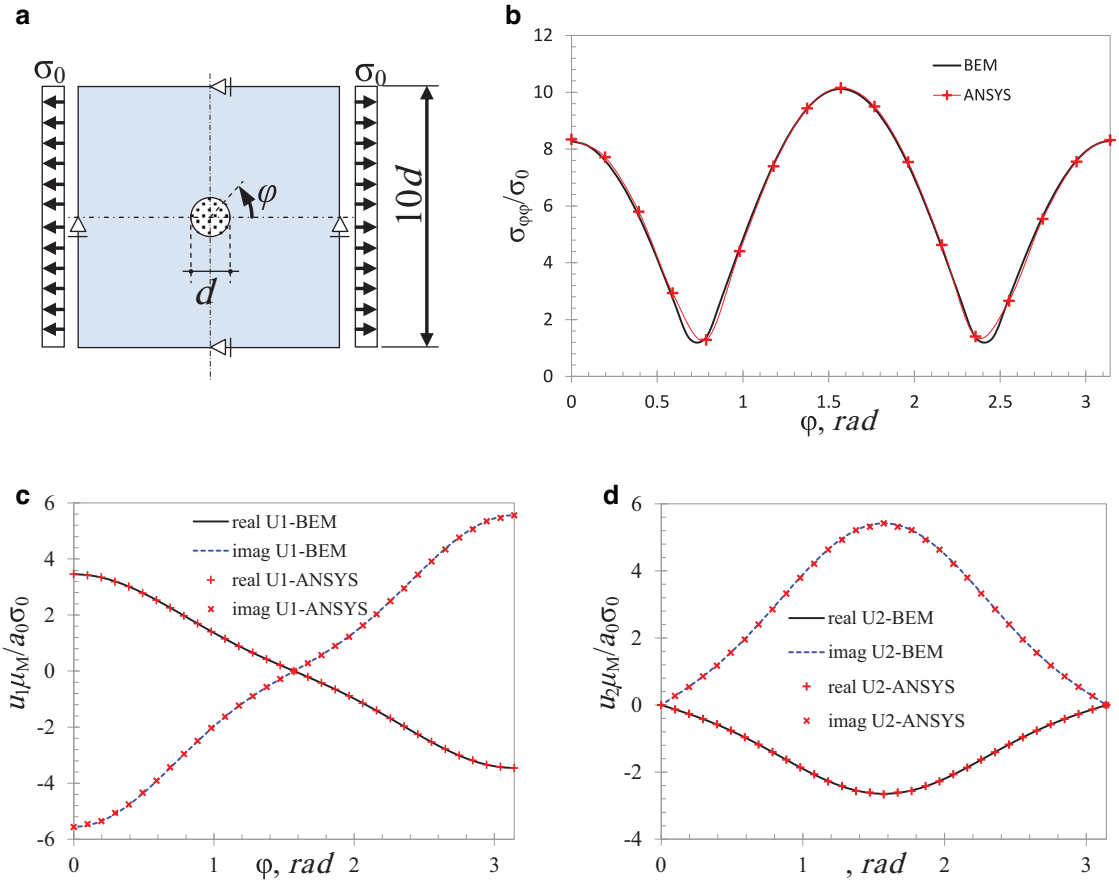


Fig. 8. Circular inclusion in a square matrix: (a) geometry and loading; (b) normalized hoop stresses at inclusion-matrix interface viewed from the matrix side; normalized (c) horizontal and (d) vertical displacement components versus polar angle, all along the inclusion contour.

matrix to those of the nano-inclusions; (c) surface properties, as quantified by the interfacial material constants; (d) dynamic interactions between multiple nano-heterogeneities, including the external boundary of the elastic matrix, and (e) frequency content of the time-harmonic loads.

7.1. Circular cavities or inclusions in a finite square matrix

We consider the reference case where the solid matrix is a square plate under time-harmonic tensile forces of magnitude σ_0 applied at the vertical sides. Fig. 12 shows the four basic configurations (Models *A, B, C, D*) involving one, three and five nano-heterogeneities. These heterogeneities are either circular cavities or inclusions of radius a_0. The size of the square plate is $10d$, with d the heterogeneity diameter. As before, the dimensionless parameter which captures interface effects at the nanoscale is defined as $s = K_S/\mu_M d$, where μ_M is the shear modulus of the matrix material. When the heterogeneity is an inclusion, then the stiffness ratio of the two material phases is $\mu_I/\mu_M = 0.2$ and their respective densities correspond to a frequency ratio of $\Omega_I/\Omega_M = 3.0$. In all simulations, the material damping is set to 5% and Poisson's ratio is 0.26 for both phases. In terms of boundary discretization, the BEM meshes used to model the perimeter of any given heterogeneity comprise 32 quadratic BE resulting in 64 nodal points. The outer perimeter of the plate is modeled by 32 BE of equal length, arranged as 8 BE along each side.

The normalized hoop stresses spectra plotted in Fig. 13 are the DSCF defined as $|\sigma_{\varphi\varphi}/\sigma_0|$ at a key point with polar angle $\varphi = \pi/2$ at the central cavity perimeter. The results for all numerical models *A–D* are presented, while four different values of the surface parameter are considered, namely $s = 0;\ 0.1;\ 0.5;\ 1.0$. The problem is solved for a normalized frequency range going up to $\Omega_M = 1$, divided into 50 equal frequency increments. For clarity, the plots are presented up to $\Omega_M = 0.8$. In addition, the results obtained by FEM using ANSYS (2009) software are also depicted in Fig. 13(a) for the case of a single circular cavity and normalized surface parameter $s = 0.5$. As before, BEM-FEM comparisons at a fixed frequency yield an excellent match, and this agreement is repeated here across the entire frequency range of interest.

Next, the DSCF for the multiple inclusions in the square matrix, arranged in the *A–D* pattern, are plotted in Fig. 14. The key point is located on the central inclusion interface with polar angle $\varphi = \pi/2$, while the hoop stresses shown are those appearing on the matrix side of the interface. As expected, the DSCF values recorded for circular inclusions are smaller compared to those recorded for cavities. The strongest amplification in the DSCF is observed at the (dimensionless) frequency range $0.20 < \Omega_M < 0.24$ for all models and for all surface parameter values. By increasing the number of heterogeneities, especially in case of cavities, we observe a shift of the first DSCF peak to the left (lower values) of this frequency range. This is so because the reduced stiffness in the composite plate leads to a lower fundamental frequency values.

Regarding the interaction effect between multiple nanoheterogeneities, as manifested by their number and configuration, the following general conclusions can now be drawn: (a) there is strong influence of the surface elasticity effects when comparing DSCF results for different values of surface elasticity parameter *s*. In fact, as surface effects become more pronounced, DSCF values drop, indicating that surface elasticity adds extra strength to the interface itself; (b)

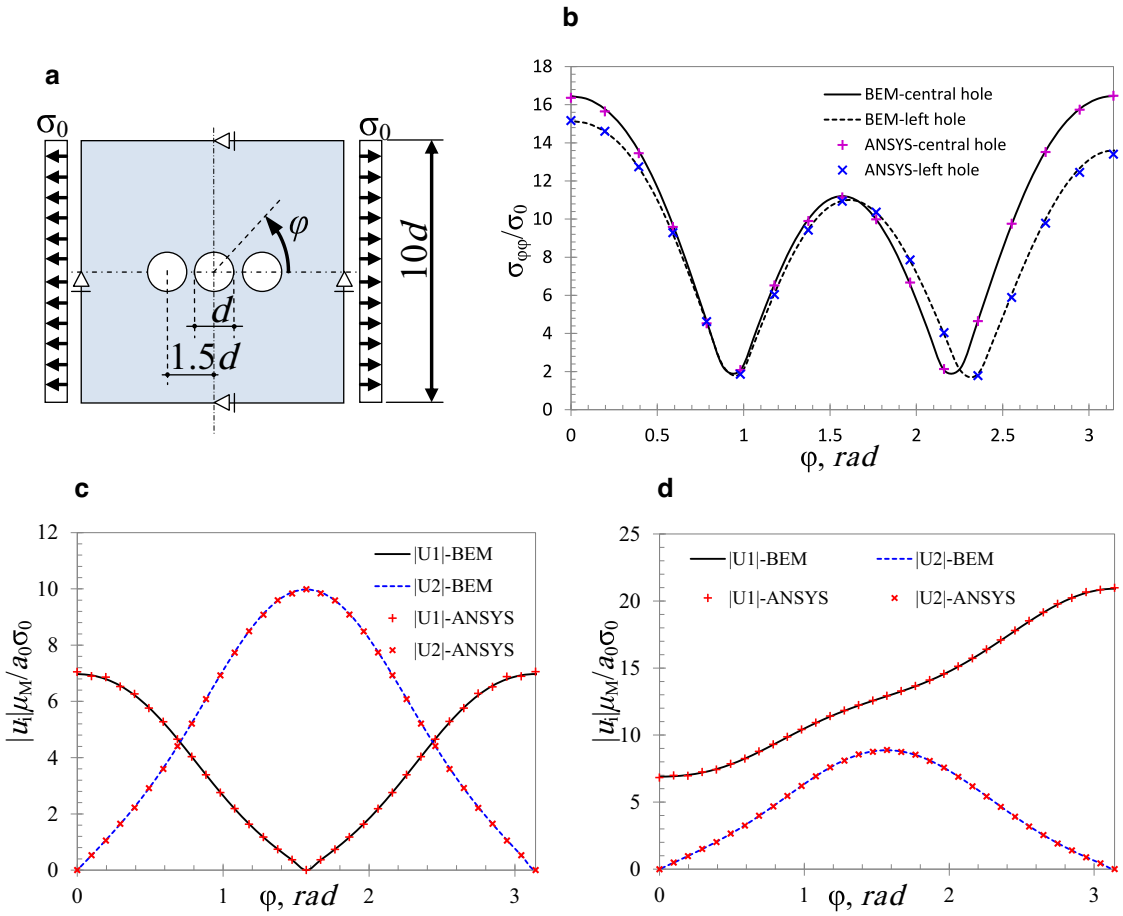


Fig. 9. Three cavities in a square matrix: (a) geometry and loading; (b) normalized hoop stresses along the central and left cavity perimeters; normalized displacement amplitudes for (c) the central cavity and (d) the left cavity.

a vertical arrangement of cavities (Model *C*) for this particular orientation of the externally applied stress field is of minor consequence, as computed DSCF values are close to those computed for the single cavity case; (c) conversely, a horizontal cavity arrangement leads to a reduction in the DSCF values as compared again to the single heterogeneity, indicating a 'shielding' effect produced by the outer two cavities; (d) when we have solid inclusions, the DSCF does not change very much for the central single inclusion, irrespective of the remaining inclusion arrangement; (e) the five cavity arrangement of Model *D*, cause considerable amplification in the DSCF at the central cavity of about 50% as compared to the single cavity case of Model *A*; This amplification is less pronounced (about 25%) when the heterogeneities are solid inclusions, cavities. More specifically, these DSCF amplification effects observed between Models *A* and *D* in the case of cavities ranges from 35% for $s = 0$ to 41% when $s = 0.5$. In the case of inclusions, the same differences drop to 31% and 9% for $s = 0$ and $s = 0.5$, respectively. Furthermore, the DSCF reduction observed between Models *A* and *B* is 41% and 28% for $s = 0$ and $s = 0.5$, respectively, when the heterogeneities are cavities. Finally, the multiple inclusion de-amplification effect that is caused to the central inclusion is about 11% when $s = 0$, while for $s = 0.5$ a small amplification of 1.7% is observed.

The next series of plots shown in Figs. 15 and 16 are for the normalized DSCF distribution along the central heterogeneity perimeter at a fixed frequency value. More specifically, Fig. 15 depicts the normalized DSCF along the central cavity perimeter for all previously considered values of the surface parameter *s* and for the four cavity configurations depicted as Models *A*–*D*. The same set of results, but for inclusions in lieu of cavities are presented in Fig. 16. The normalized frequency for the case of inclusions is defined as $\Omega = \Omega_{M,}$ while the numerical value selected in all plots corresponds to the first peak in the DSCF, as reported in Figs. 13 and 14. The stress distribution along the entire interface allows for a better assessment of the interaction effects between the cavities or the inclusions. Although the horizontal cavity arrangement of Model *B* leads to a reduction in the DSCF value at polar angle$\varphi = \pi/2$, an amplification is observed at the equator ($\varphi = 0$ and $\varphi = \pi$) due to the presence of neighbouring cavities close to these points, see Fig. 15(b). Moreover the influence of the surface parameter *s* is not as straightforward as it is for the single cavity case in Fig. 15(a). For $s = 0.1$, both amplification and de-amplification effects are manifested along the cavity perimeter in Fig. 15(b) as compare to the absence of surface effect ($s = 0$), which indicates that strong molecular surface action overrides the classical mechanical effects observed at the macro-scale.

7.2. Elliptical cavities in a finite square matrix

The aim of this final sequence of numerical simulations is to examine the influence of the cavity shape on the DSCF. The square matrix domain now contains elliptical, horizontally or vertically elongated cavities arranged in the same geometrical configuration as before and involving one, three (row or column), and five cavities. The semi-axes are chosen so that $a + b = d$ and their ratio is $a/b = 2$ for horizontally elongated and $a/b = 0.5$ for vertically elongated cavities, respectively (see Figs. 17 and 18). The centre-to-centre distance between ellipses is 1.5*d*, as was shown in Fig. 12 and the size of the square plate is 10*d*. The square plate itself is subjected to uniaxial tension in the horizontal direction, as in all previous simulations. The

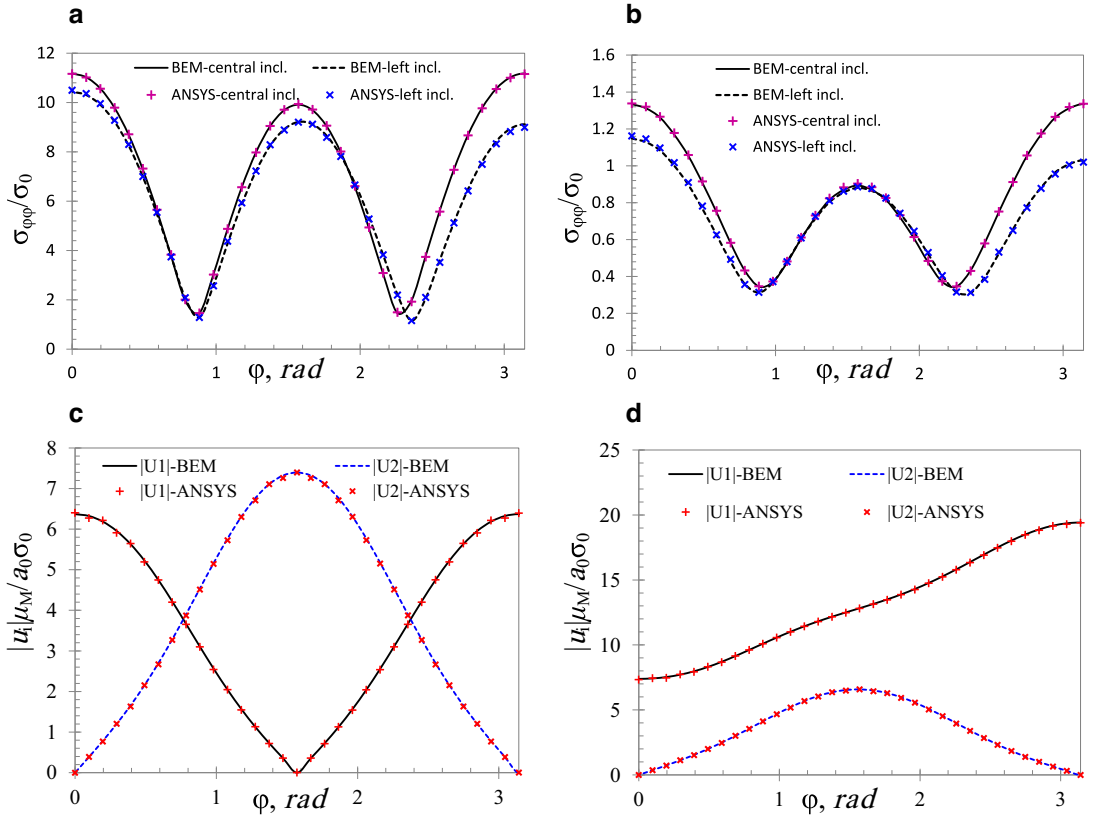


Fig. 10. Three inclusions in a square matrix: normalized hoop stresses at central and left inhomogeneity interfaces viewed from (a) the matrix side and (b) the inclusion side; normalized displacement amplitudes at (c) the central inclusion and (d) the left inclusion.

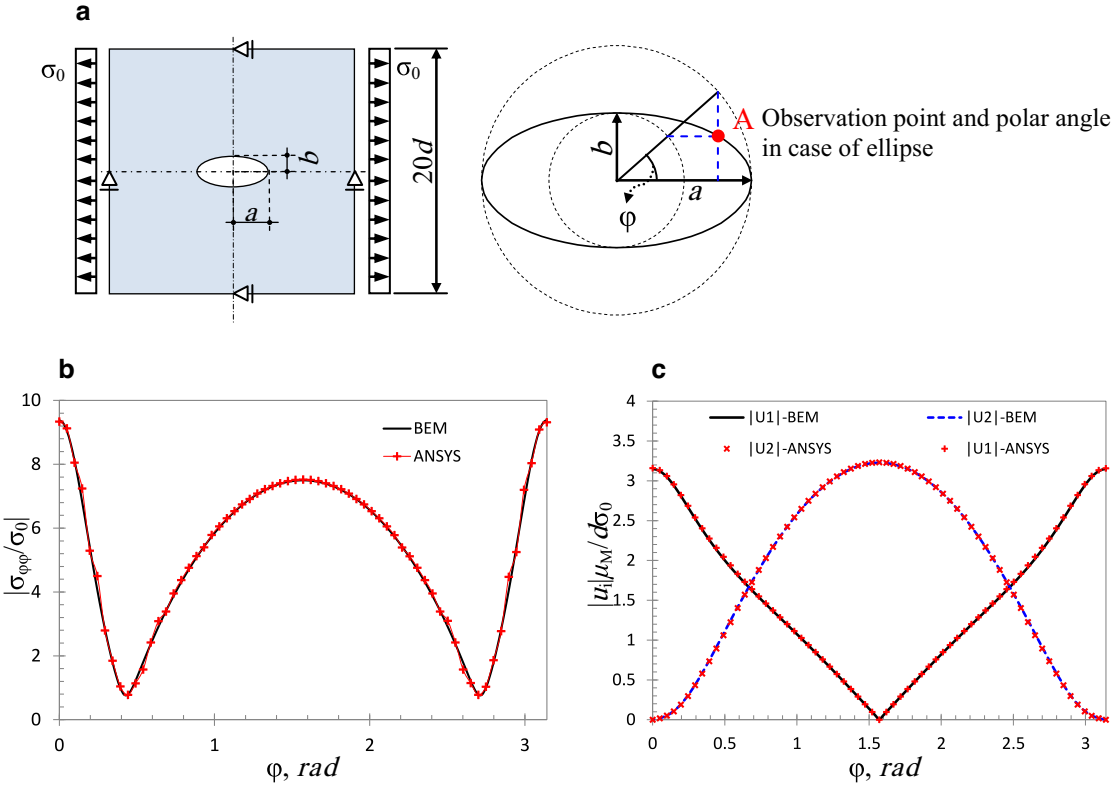


Fig. 11. Single elliptic cavity in a square matrix: (a) geometry and loading; (b) normalized hoop stresses and (c) displacement amplitudes at the cavity perimeter.

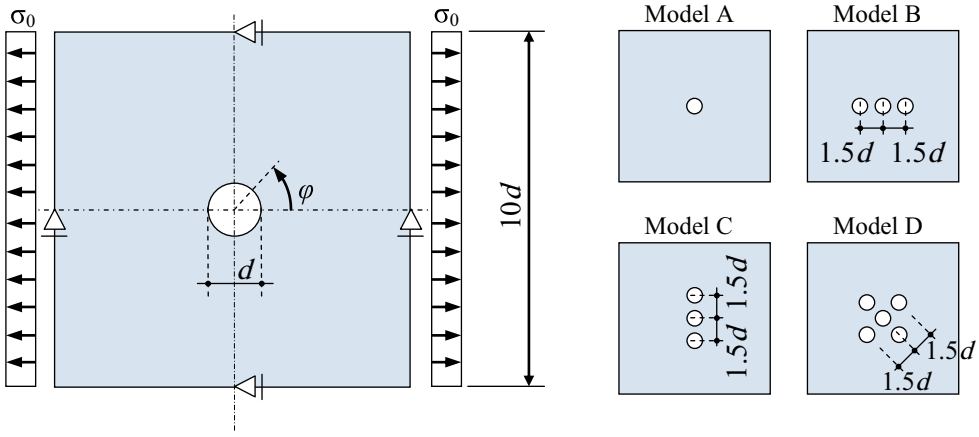


Fig. 12. Elastic plate with various cavity and inclusion configurations: geometry, dimensions and layouts for Models *A–D*.

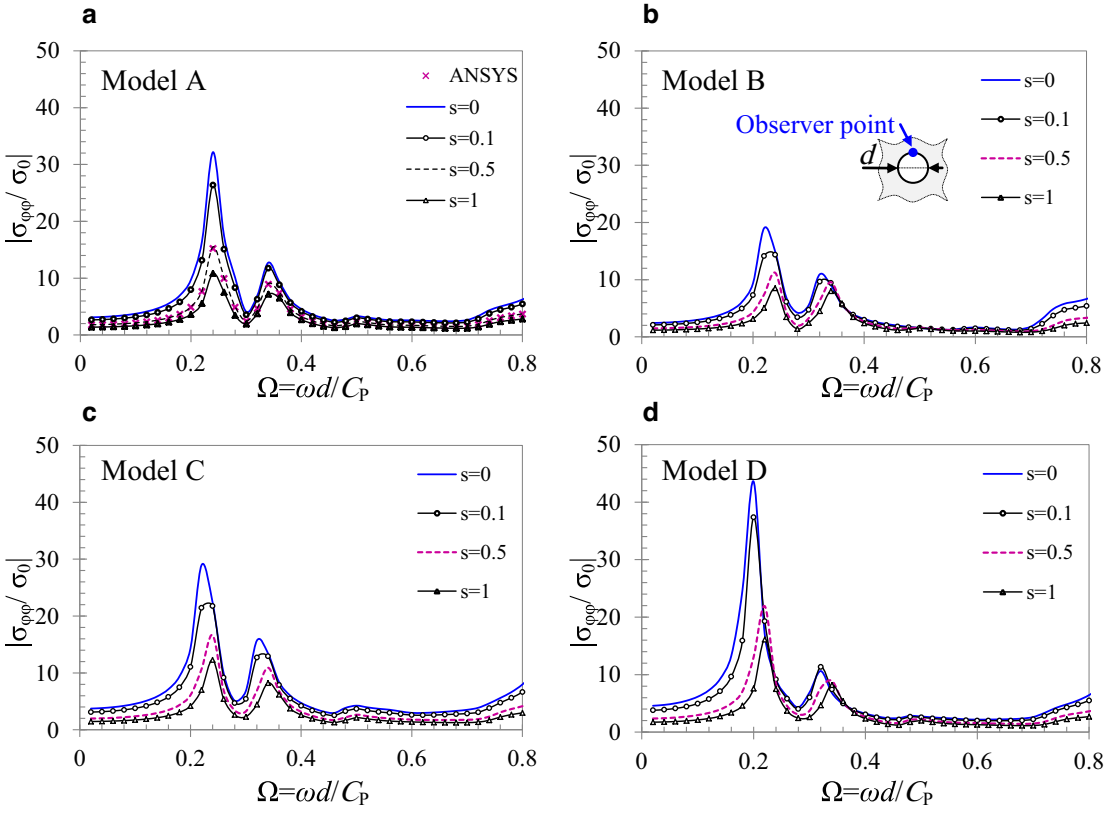


Fig. 13. DSCF for (a)–(d) cavity Models *A–D*, respectively, at observer point $\varphi = \pi/2$on the central cavity perimeter.

dimensionless parameter which captures interface effects at the nano-scale, namely $s = K_S/(\mu_M d)$ is set equal to $s = 0.5$.

More specifically, the normalized DSCF for the central cavity and the four aforementioned configurations is plotted versus normalized frequency at observer points with polar angles $\varphi = \pi/2$ and $\varphi = 0$ along the perimeter in order to cover the behaviour of sharpest edge and the smoothest part of the cavity. As previously mentioned, results associated with the horizontally elongated ellipses are plotted in Fig. 17 and those for the vertically elongated in Fig. 18. The subplots of Figs. 17(a) and 18(a) give the frequency variation of the DSCF for an observation point located at polar angle for $\varphi = \pi/2$, while Figs. 17(b) and 18(b) are similar plots for observation point with polar angle $\varphi = 0$. Finally, Figs. 17(c) and 18(c) are the polar distributions of normalized hoop stresses, for horizontally and vertically elongated ellipses respectively, along the central cavity perimeter for a fixed frequency value corresponding to the first peak of the immediately previous frequency plots. All results point to a strong interaction effect between the elliptical cavities, irrespective of their orientation. Also, for a tension field in the horizontal direction of the solid matrix, it is the horizontally arranged elliptic cavities that consistently produce higher DSCF values, but the critical frequencies of vibration are roughly two, namely $\Omega \sim 0.25$ and $\Omega \sim 0.35$. In terms of the spatial distribution of the DSCF, the critical point is the apex (sharp edge) of the cavity, a conclusion that is expected. What is somewhat surprising, however, is that the presence of multiple cavities in the vicinity of the centrally-placed one, cause both amplification and de-amplification effects, depending on their number and their geometric orientation.

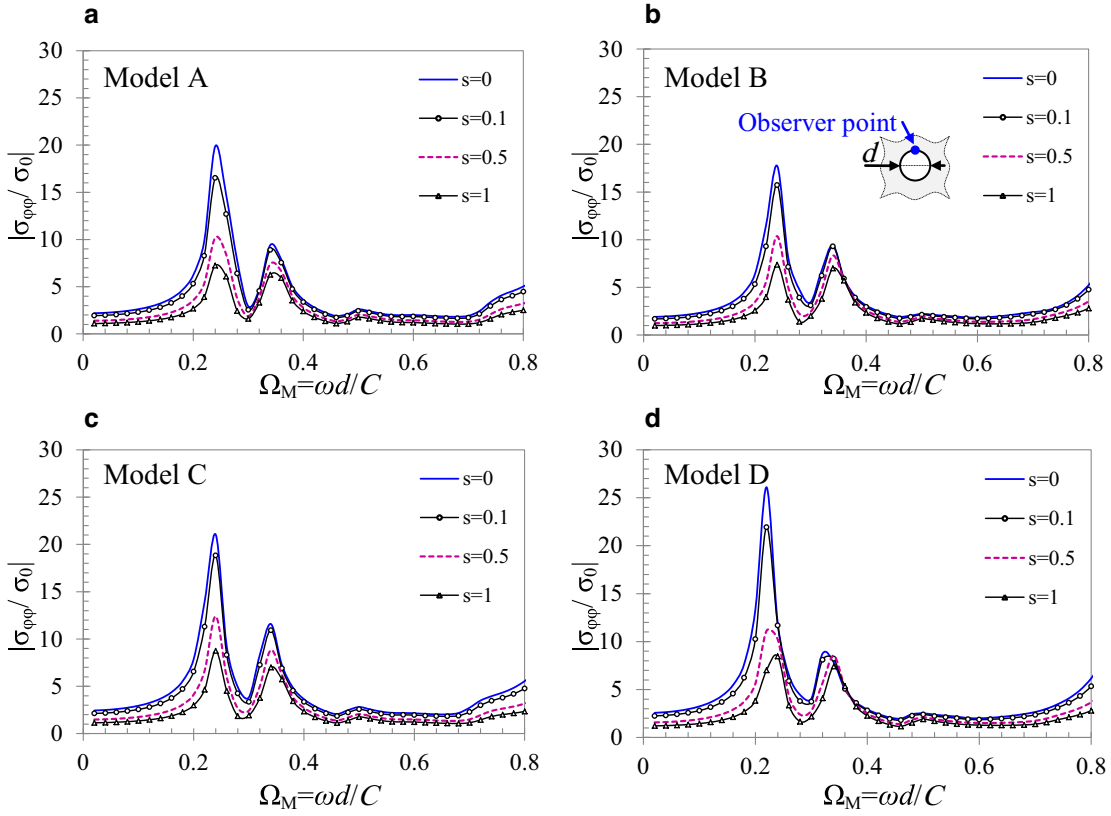


Fig. 14. DSCF for (a)–(d) inclusion Models *A*–*D*, respectively, at observer point $\varphi = \pi/2$on the central inclusion interface viewed from the matrix side.

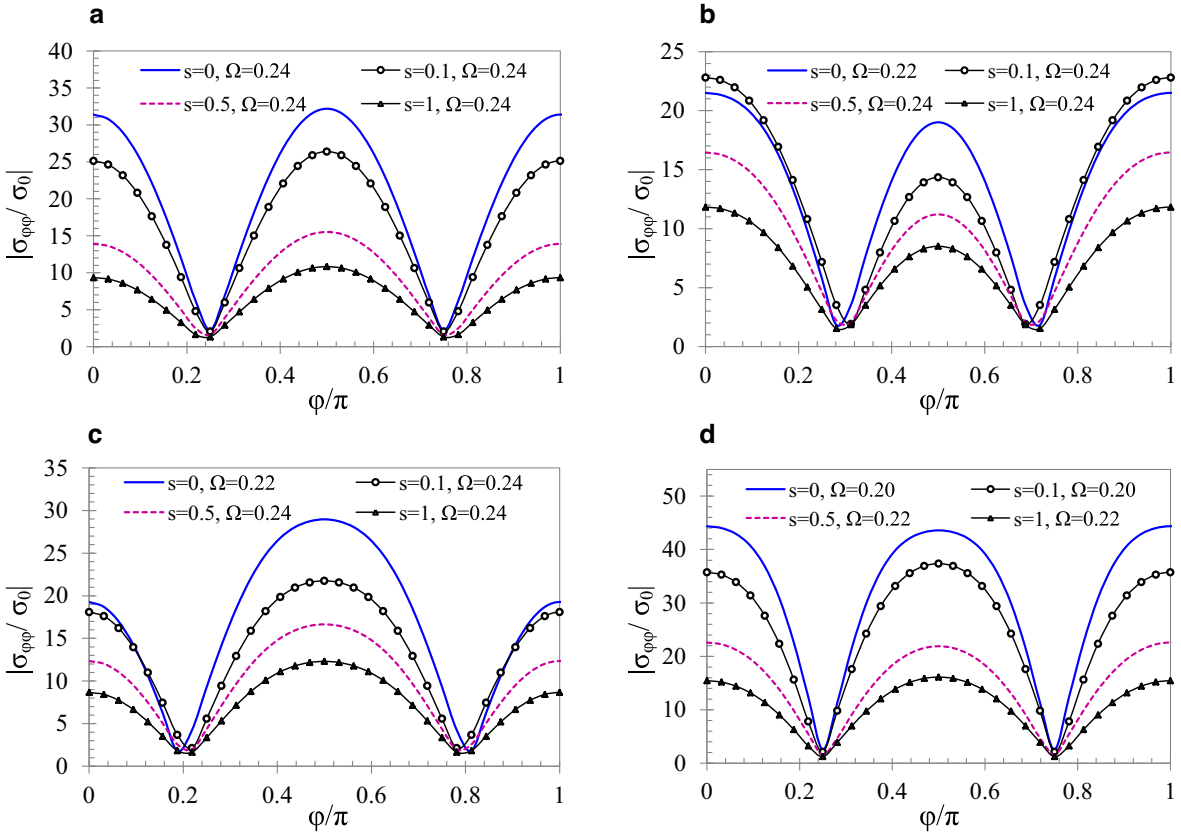


Fig. 15. Polar angle distribution of the DSCF for cavities at a fixed frequency value corresponding to the maximum amplification for: (a) Model *A*; (b) Model *B*; (c) Model *C*; (d) Model *D*.

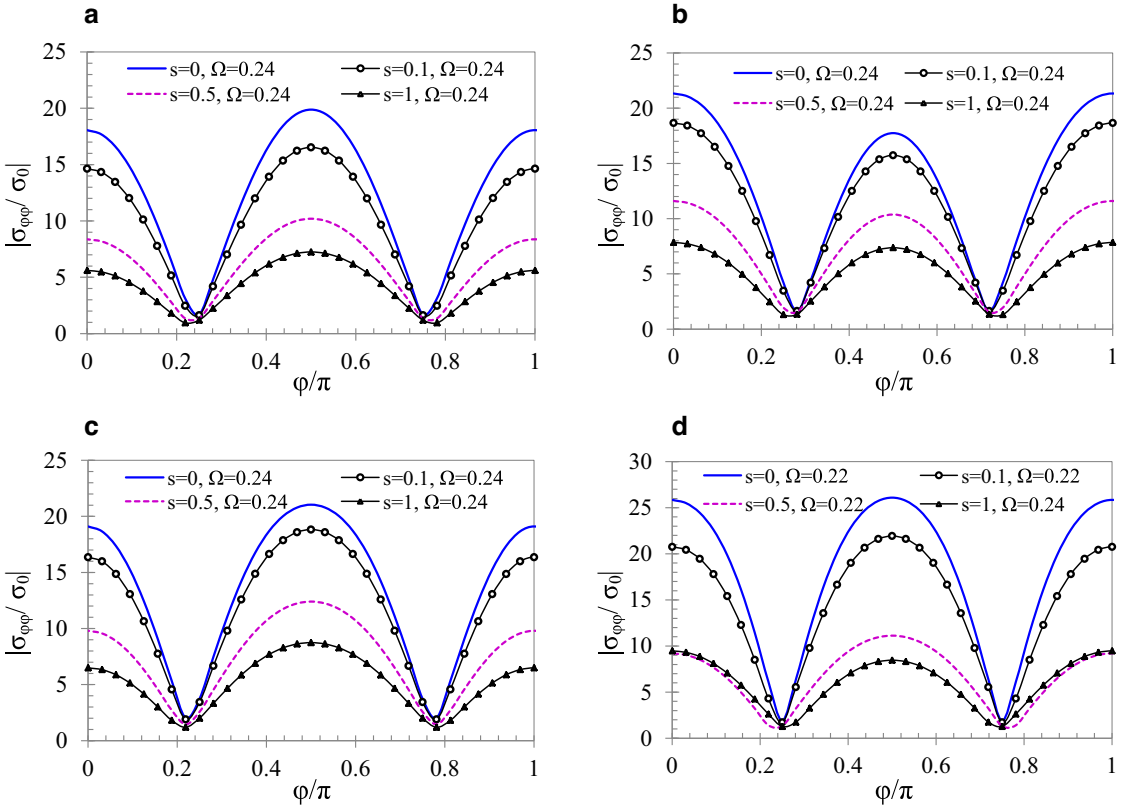


Fig. 16. Polar angle distribution of the DSCF for inclusions at a fixed frequency value corresponding to the maximum amplification for: (a) Model *A*; (b) Model *B*; (c) Model *C*; (d) Model *D*.

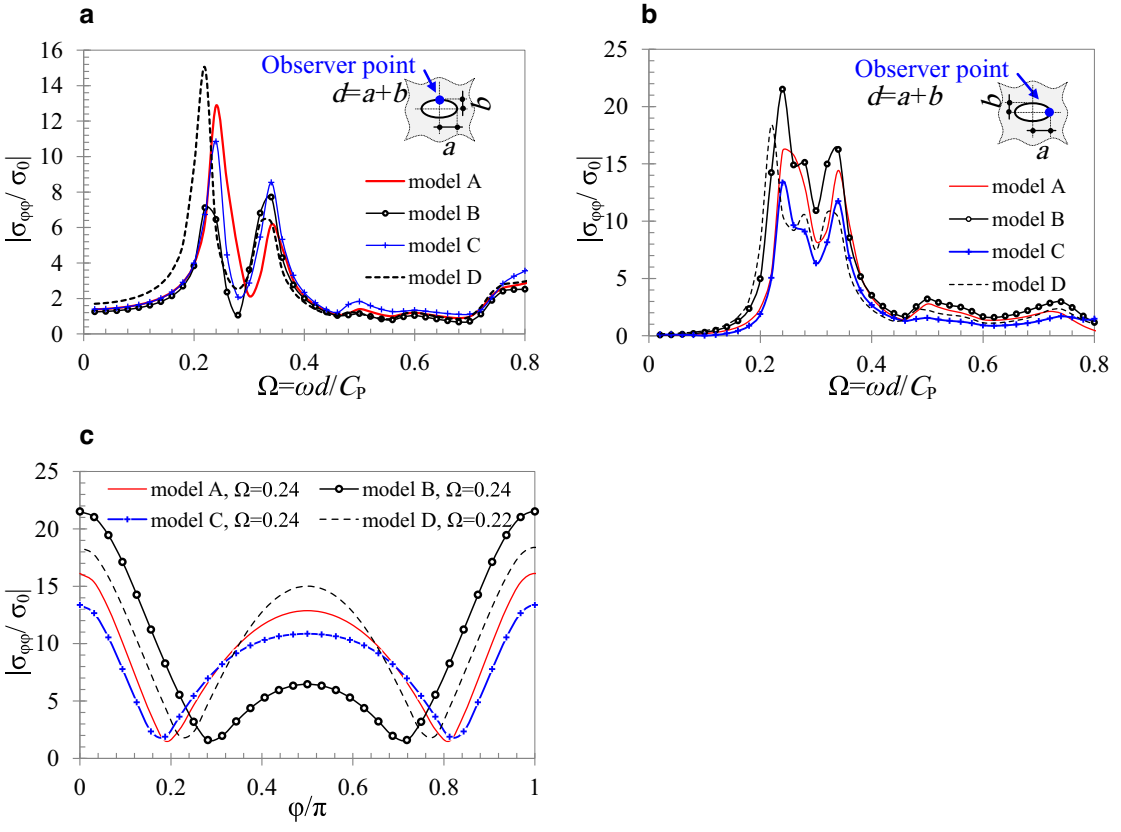


Fig. 17. Horizontally elongated elliptical cavities with a semi-axes ratio $a/b = 2$ and surface parameter value of s=0.5: DSCF versus normalized frequency for Models *A*–*D* at the central cavity and at observer points (a) $\varphi = \pi/2$and (b) $\varphi = 0$; (c) polar angle distribution of the DSCF at fixed frequency.

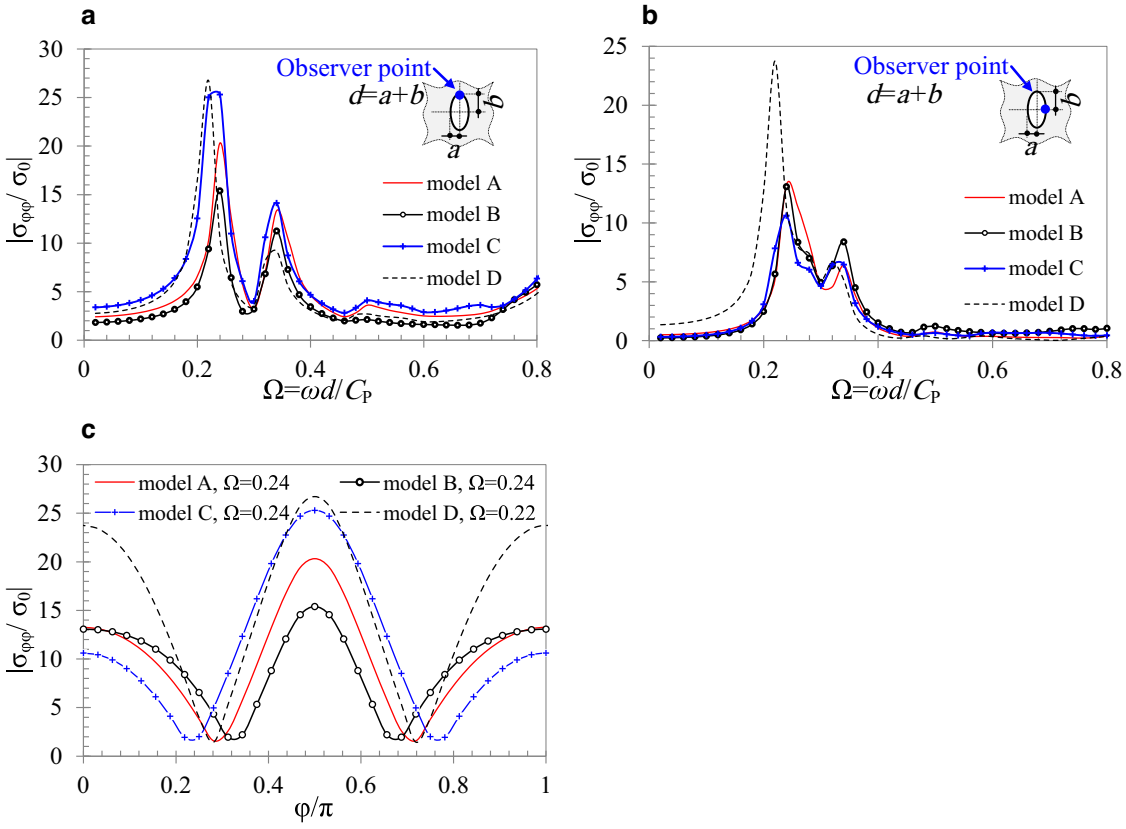


Fig. 18. Vertically elongated elliptical cavities with a semi-axes ratio $a/b = 0.5$ and surface parameter value of $s = 0.5$: DSCF versus normalized frequency for Models *A–D* at the central cavity and at observer points (a) $\varphi = \pi/2$and (b) $\varphi = 0$; (c) polar angle distribution of the DSCF at fixed frequency.

8. Conclusions

In this work, we present two computational tools for the solution of 2D elastodynamic problems involving a finite-sized elastic matrix at the nano-scale containing multiple heterogeneities of arbitrary type, shape, size, number and geometrical configuration. More specifically, these tools are based on frequency-dependent BEM and FEM formulations. The former is a complete formulation, while in the latter case we develop a macro-finite element which is implemented within the ANSYS (2009) software package. In both cases, due consideration is given to the surface elasticity effect, as expressed by non-classical boundary conditions proposed in the surface elasticity theory of Gurtin and Murdoch (1975). These two numerical schemes were first verified, then compared to each other and finally used for numerical parametric studies. The numerical results produced serve to quantify the non-uniform stress distribution in the solid matrix and the zones of pronounced dynamic stress concentration around the cavity/inclusion perimeters.

The basic conclusion that can be drawn from the numerical simulations is that dynamic stress concentration phenomena at the mechanical nanoscale are sensitive to a number of key factors (or problem parameters), namely: (a) The type of heterogeneities (be it a cavity or a solid inclusion), (b) their size (macro or nano scales), (c) the interface material parameter values, (d) the shape, number and configuration of the heterogeneities embedded in the elastic solid matrix, (e) the type of dynamic interaction which develops between the heterogeneities themselves and the perimeter of the bounded solid matrix and finally (f) the type of applied external loads. Of course, it is necessary to have available the range of numerical values for the mechanical properties of heterogeneous nanocomposite materials, which are either provided by the manufacturer or made available following material testing by specialized laboratories. In sum, the present combination of classical elastodynamic theory with non-classical boundary conditions within the framework of Gurtin–Murdoch surface elasticity theory, has the potential to (a) quantify size effects at the nano-scale, (b) help optimize the design of nanocomposites and (c) to maximize their performance under operating conditions.

Acknowledgment

The authors acknowledge support by the Bulgarian NSF under Grant No. DFNI-I02/12.

References

ANSYS, 2009. Release 10.0, Structural Mechanics Package. Canonsburg, Pennsylvania.
Achenbach, J.D., 1973. Wave Propagation in Elastic Solids. North Holland, Amsterdam.
Ayatollahi, M., Fariborz, S.J., Najafabadi, A.M., 2009. Anti-plane elastodynamic analysis of planes with multiple defects. Appl. Math. Model. 33, 663–676. doi:10.1016/j.apm.2007.11.031.
Babich, V.M., 1956. Ray Methods for Computation of the Intensity of Wavefronts. Nauka Publications, Moscow.
Berezovski, M., 2010. Numerical Simulation of Wave Propagation in Heterogeneous and Microstructured Materials (Dissertation). TUT Press, Tallinn, Estonia ISSN: 1406-4723, ISBN: 978-9985-59-998-3.
Boore, D.M., 1972. Finite-difference methods for seismic wave propagation in heterogeneous materials. In: Bolt, B.A. (Ed.), Methods in Computational Physics. Academic Press, New York, pp. 1–37 Volume 11 of Seismology: Surface waves and Earth Oscillations.
Boström, A., 2003. Review of hypersingular integral equation method for crack scattering and application to modeling of ultrasonic nondestructive evaluation. Appl. Mech. Rev. 56 (4), 383–405.
Dineva, P., Wuttke, F., Manolis, G.D., 2012. Elastic wave scattering and stress concentration effects in non-homogeneous poroelastic geological media with discontinuities. Soil Dyn. Earthq. Eng. 41, 102–118.
Dominguez, J., 1993. Boundary Elements in Dynamics. CMP, Southampton.
Dong, C.Y., Pan, E., 2011. Boundary element analysis of nanoinhomogeneities of arbitrary shapes with surface and interface effects. Eng. Anal. Bound. Elem. 35, 996–1002.

Dravinski, M., Yu, M.C., 2011. Scattering of plane harmonic SH-waves by multiple inclusions. Geophys. J. Int. 186, 1331–1346.
Fah, D., 1992. A hybrid technique for the estimation of strong ground motion in sedimentary basins (PhD Thesis), ETH Publication no. 9767, Swiss Federal Institute of Technology, Zurich.
Fang, X.Q., Liu, J.X., Yang, S.P., Zhang, L.L., 2010. Effect of surface/interface on the dynamic stress of two interacting cylindrical nano-inhomogeneities under compressional waves. Thin Solid Films 518, 6938–6944.
Gatmiri, B., Arson, C., 2008. Seismic site effects by an optimized 2D BE/FE method. II. Quantification of site effects in two-dimensional sedimentary valleys. Soil Dyn. Earthq. Eng. 28, 646–661.
Gatmiri, B., Arson, C., Nguyen, K.V., 2008. Seismic site effects by an optimized 2D BE/FE method I. Theory, numerical optimization and application to topographical irregularities. Soil Dyn. Earthq. Eng. 28, 632–645.
Grekov, M., Morozov, N., 2012. Surface effects and problems of nanomechanics. J. Ningbo Univ. 25 (1), 60–63.
Gurtin, M.E., Murdoch, A.I., 1975. A continuum theory of elastic material surfaces. Arch. Ration. Mech. Anal. 57, 291–323.
Jing, G.Y., Duan, H.L., Sun, X.M., Zhang, Z.S., Xu, J., Y.D., Wang, J.X., Yu, D.P., 2006. Surface effects on elastic properties of silver nanowires: Contact atomic-force microscopy. Phys. Rev. B 73, 235409.
Kausel, E., 2006. Fundamental Solutions in Elastodynamics: A Compendium. Cambridge University Press, Cambridge.
Kennett, B.L.N., 1983. Seismic Wave Propagation in Stratified Media, I. Cambridge University Press, Cambridge.
Kobayashi, S., 1983. Some problems of the boundary integral equation method in elastodynamics. In: Brebbia, C.A., Futagami, T., Tanaka, M. (Eds.), Proceedings of the Fifth International Boundary Element Method Conferences. Springer-Verlag, Berlin, pp. 775–784.
Komatitsch, D., Erlebacher, G., Göddeke, D., Michéa, D., 2010. High-order finite-element seismic wave propagation modeling with MPI on a large GPU cluster. J. Comp. Phys. 229, 7692–7714.
Kratochvil, J., Becker, W., 2012. Asymptotic analysis of stresses in an isotropic linear elastic plane or half-plane weakened by a finite number of holes. Arch. Appl. Mech. 82 (6), 743–754.
Kristek, J., Moczo, P., 2003. Seismic-wave propagation in viscoelastic media with material discontinuities: A 3D fourth-order staggered-grid finite-difference modelling. Bull. Seism. Soc. Am. 93, 2273–2280.
Li, W., 2004. Analytical Solutions and Numerical Simulation of the Scattering Plane Waves by Local Sites with Saturated Soil (Doctoral Dissertation). Beijing Jiaotong University, Beijing, P. R. China.
Liu, D., Gai, B., Tao, G., 1982. Applications of the method of complex functions to dynamic stress concentrations. Wave Mot. 4, 293–304.
Lu, J., Hanyga, A., 2004. Dynamic interaction between multiple cracks and a circular hole. Int. J. Solids Struct. 41, 6725–6744.
Manolis, G.D., Beskos, D.E., 1988. Boundary Element Methods in Elastodynamics. Allen and Unwin, London.
Manolis, G., Parvanova, S., Makra, K., Dineva, P., 2015. Seismic response of buried metro tunnels by a hybrid FDM-BEM approach. Bull. Earthq. Eng. 13, 1953–1977.
Manolis, G., Dineva, P., 2015. Elastic waves in continuous and discontinuous geological media by boundary integral equation methods: A review. Soil Dyn. Earthq. Eng. 70, 11–29.
Miller, R.E., Shenoy, V.B., 2000. Size-dependent elastic properties of nanosized structural elements. Nanotechnology 11, 139–147.
Mogilevskaya, S.G., Crouch, S.L., 2001. A Galerkin boundary integral method for multiple circular elastic inclusions. Int. J. Numer. Methods Eng. 52, 1069–1106.
Mogilevskaya, S.G., Crouch, S.L., 2002. A Galerkin boundary integral method for multiple circular elastic inclusions with homogeneously imperfect interfaces. Int. J. Solids Struct. 39 (18), 4723–4746.
Nakasone, Y., Nishiyama, H., Nojiri, T., 2000. Numerical equivalent inclusion method: a new computational method for analysing stress fields in and around inclusions of various shapes. Mater. Sci. Eng. A285, 229–238.
Panza, G., Paskaleva, I., Dineva, P., LaMura, C., 2009. Earthquake site effects modeling by hybrid MS-BIEM: The case study of Sofia Bulgaria. Rendiconti di Scienze Fisiche, Accademia dei Lincei 20, 91–116.
Pao, Y.H., Gajewski, R.R., 1977. The generalized Ray theory and transient responses of layered elastic solids. Phys. Acoust. 13, 183–265.
Pao, Y.H., Mow, C.C., 1971. Diffraction of Elastic Waves and Dynamic Stress Concentration. Crane Russak, New York.
Parvanova, S.L., Dineva, P.S., Manolis, G.D., 2013. Dynamic behavior of a finite-sized elastic solid with multiple cavities and inclusions using BIEM. Acta Mech 224 (3), 597–618.
Parvanova, S., Dineva, P., Manolis, G., Kochev, P., 2014. Dynamic response of a solid with multiple inclusions under anti-plane strain conditions by the BEM. Comput. Struct. 139, 65–83.
Parvanova, S., Manolis, G., Dineva, P., 2015. Wave scattering by nanoheterogeneities embedded in an elastic matrix via BEM. Eng. Anal. Bound. Elem. 56, 57–69.
Ru, Y., Wang, G.F., Wang, T.J., 2009. Diffraction of elastic waves and stress concentration near a cylindrical nano-inclusion incorporating surface effect. J. Vib. Acoust. 13 061011-1-061011-7.
Santare, M.H., Thamburaj, P., Gazonas, G.A., 2003. The use of graded finite elements in the study of elastic wave propagation in continuously nonhomogeneous materials. Int. J. Solids Struct. 40, 5621–5634.
Sendova, T., Walton, G.R., 2010. A New approach to the modeling and analysis of fracture through extension of continuum mechanics to the nanoscale. Math. Mech. Solids 15 (3), 368–413.
Shenoy, VB., 2002. Size-dependent rigidities of nanosized torsional elements. *Int. J. Solids Struct*. 39, 4039–4052.
Tian, L., 2006. *Analytical and finite element solutions for an elastic matrix with two-dimensional nanoscale inhomogeneities (Thesis for Master of Applied Science)*, University of British Columbia, Vancouver, http://hdl.handle.net/2429/18383
Tian, L., Rajapakse, R.K.N.D., 2007. Elastic field of an isotropic matrix with a nanoscale elliptical inhomogeneity. *Int. J. Solids Struct*. 44, 7988–8005.
Valeva, V., Ivanova, J., 1998. Strength numerical analysis of a composite material with holes. In: Yu, M.H., Fan, S.G. (Eds.), Strength Theory: Application, Development and Prospects for 21st Century. Science Press, New York and Beijing, pp. 359–364.
Vasilev, G., Parvanova, S., Dineva, P., Wuttke, F., 2015. Soil-structure interaction using BEM-FEM coupling through ANSYS software package. Soil Dyn. Earthq. Eng. 70, 104–117.
Wang, G.F., Wang, T.J., Feng, X.Q., 2006. Surface effects on the diffraction of plane compressional waves by a nanosized circular hole. Appl. Phys. Lett. 89, 231923-1–231923-3.
Wang, G.F., 2009. Multiple diffraction of plane compressional waves by two circular cylindrical holes with surface effects. J. Appl. Phys. 105, 013507-1–013507-6.
Wang, W., Zeng, X., Ding, J., 2010. Finite element modeling of two dimensional nanoscale structures with surface effects. World Acad. Sci., Eng. Technol. 4, 12–20.
Wolf, J.P., Song, C., 1996. Finite Element Modeling of Unbounded Media. Wiley, Somerset, UK.
Wolf, J.P., 2003. The Scaled Boundary Finite Element Method. Wiley, Somerset, UK.
Yang, Z., Hei, B., Wang, Y., 2015. Scattering by circular cavity in radially inhomogeneous medium with wave velocity variation. Appl. Math. Mech. 36 (5), 599–608 (English Edition).
Zhang, J., Katsube, N., 1995. A hybrid finite element method for heterogeneous materials with randomly dispersed elastic inclusions. Finite Elem. Anal. Des. 19, 45–55.
Zhang, Q.F., Wang, G.F., Schiavone, P., 2011. Diffraction of plane compressional waves by an array of nanosized cylindrical holes. J. Appl. Mech. 78 021003-1-021003-5.